Article

Observation of plaid-like spin splitting in a noncoplanar antiferromagnet

https://doi.org/10.1038/s41586-024-07023-w

Received: 26 March 2023

Accepted: 3 January 2024

Published online: 14 February 2024

Check for updates

Yu-Peng Zhu[1,11], Xiaobing Chen[1,11], Xiang-Rui Liu[1], Yuntian Liu[1], Pengfei Liu[1], Heming Zha[2], Gexing Qu[3], Caiyun Hong[4], Jiayu Li[1], Zhicheng Jiang[2], Xiao-Ming Ma[1], Yu-Jie Hao[1], Ming-Yuan Zhu[1], Wenjing Liu[2], Meng Zeng[1], Sreehari Jayaram[5,6,7], Malik Lenger[5,6,7], Jianyang Ding[2], Shu Mo[1], Kiyohisa Tanaka[8], Masashi Arita[9], Zhengtai Liu[2], Mao Ye[2], Dawei Shen[2], Jörg Wrachtrup[5,6,7], Yaobo Huang[10], Rui-Hua He[4], Shan Qiao[2]✉, Qihang Liu[1]✉ & Chang Liu[1]✉

Spatial, momentum and energy separation of electronic spins in condensed-matter systems guides the development of new devices in which spin-polarized current is generated and manipulated[1–3]. Recent attention on a set of previously overlooked symmetry operations in magnetic materials[4] leads to the emergence of a new type of spin splitting, enabling giant and momentum-dependent spin polarization of energy bands on selected antiferromagnets[5–10]. Despite the ever-growing theoretical predictions, the direct spectroscopic proof of such spin splitting is still lacking. Here we provide solid spectroscopic and computational evidence for the existence of such materials. In the noncoplanar antiferromagnet manganese ditelluride ($MnTe_2$), the in-plane components of spin are found to be antisymmetric about the high-symmetry planes of the Brillouin zone, comprising a plaid-like spin texture in the antiferromagnetic (AFM) ground state. Such an unconventional spin pattern, further found to diminish at the high-temperature paramagnetic state, originates from the intrinsic AFM order instead of spin–orbit coupling (SOC). Our finding demonstrates a new type of quadratic spin texture induced by time-reversal breaking, placing AFM spintronics on a firm basis and paving the way for studying exotic quantum phenomena in related materials.

Historically, mechanisms for splitting a spin-degenerate energy band (Fig. 1a) include Zeeman interaction[11], in ferromagnets, in which electrons with different spins are equally separated in energy regardless of their momenta (Fig. 1b), and Rashba–Dresselhaus interaction[12,13], in which the spins split in a momentum-dependent manner in nonmagnetic crystals lacking inversion symmetry (Fig. 1d). Recently, a new type of spin splitting induced by the long-range magnetic order has been predicted in certain antiferromagnets, even when SOC is absent (Fig. 1c). Such proposal enables the choice of light-element materials for generation of, for example, spin currents[14–17] and tunnelling magnetoresistance effect[18–22], substantially widening the scope of AFM spintronics[23,24].

Instead of the well-studied (magnetic) space groups, the symmetry operations allowed in these new magnets are fully described by an enhanced symmetry group called spin space group[4,25–32], in which the decoupling of lattice rotation and spin rotation permits certain symmetry operations that are excluded by conventional magnetic space groups, leading to exotic physical phenomena such as weak-SOC Z_2 topological phases[4], chiral Dirac-like fermions[33,34], C-pair spin valley locking[35] and anomalous Hall effect[7,36,37]. The appearance of AFM-induced spin splitting is unique in that its splitting scale depends on the momentum of the electrons and can be much larger than the largest known Rashba effect[38]. The collinear members of these antiferromagnets are named 'altermagnets' in the literature[9,39], although such unconventional spin splitting can also take place in noncollinear magnets[6].

Despite the thriving theoretical studies on these new magnets[4,6–10] and transport evidence on one of them[15–17,36], the direct spectroscopic proof of such spin splitting itself is lacking. Here, using spin-resolved and angle-resolved photoemission spectroscopy (SARPES) measurements and theoretical analysis, we demonstrate unambiguously the existence of this AFM-induced spin-splitting effect on a noncoplanar antiferromagnet, $MnTe_2$. By virtue of the state-of-the-art SARPES facilities[40,41], we observe that the in-plane components of the spin on a bulk band are antisymmetric about both horizontal and vertical high-symmetry planes. Thus, the spin texture forms a plaid pattern in

[1]Department of Physics and Shenzhen Institute for Quantum Science and Engineering (SIQSE), Southern University of Science and Technology (SUSTech), Shenzhen, China. [2]National Key Laboratory of Materials for Integrated Circuits, Shanghai Institute of Microsystem and Information Technology, Chinese Academy of Sciences, Shanghai, China. [3]Beijing National Laboratory for Condensed Matter Physics, Institute of Physics, Chinese Academy of Sciences, Beijing, China. [4]Key Laboratory for Quantum Materials of Zhejiang Province, Department of Physics, Westlake University, Hangzhou, China. [5]3rd Institute of Physics, University of Stuttgart, Stuttgart, Germany. [6]Center for Integrated Quantum Science and Technology (IQST), University of Stuttgart, Stuttgart, Germany. [7]Center for Applied Quantum Technology, University of Stuttgart, Stuttgart, Germany. [8]Institute for Molecular Science, National Institutes of Natural Sciences, Okazaki, Japan. [9]Hiroshima Synchrotron Radiation Center, Hiroshima University, Higashi-Hiroshima, Japan. [10]Shanghai Synchrotron Radiation Facility, Shanghai Advanced Research Institute, Chinese Academy of Sciences, Shanghai, China. [11]These authors contributed equally: Yu-Peng Zhu, Xiaobing Chen. ✉e-mail: qiaoshan@mail.sim.ac.cn; liuqh@sustech.edu.cn; liuc@sustech.edu.cn

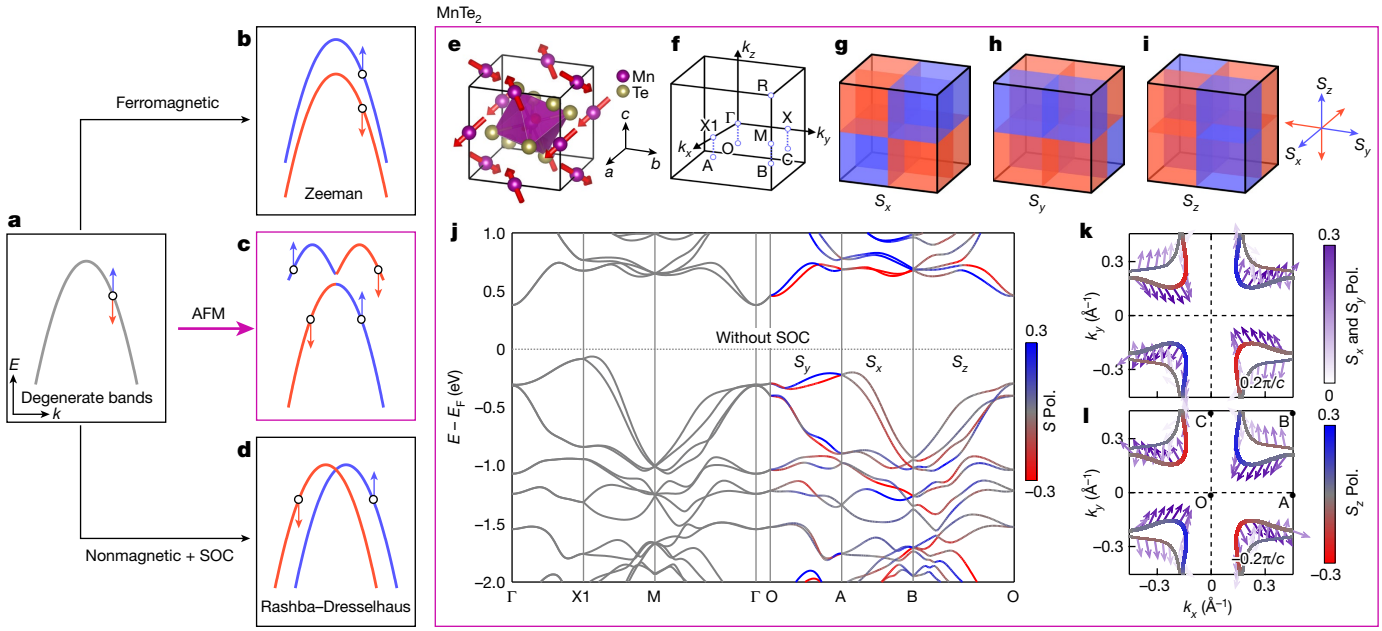

Fig. 1 | Different prototypes of spin-splitting effect and DFT calculation results of $MnTe_2$. a–d, Schematics of the spin-degenerate bands and spin splitting induced by the Zeeman effect, AFM order and spin–orbit interaction with structural asymmetry. Blue and red denote opposite spins. **e**, Crystal structure of $MnTe_2$. The noncoplanar magnetic configuration of Mn atoms is indicated by the red arrows. Magnetic moments of about $4.3\mu_B$ are arranged along the bulk diagonal direction. **f**, The first Brillouin zone of $MnTe_2$. The O–A–B–C plane is the $k_z = -0.2\pi/c$ plane, corresponding to the plane of our ARPES and SARPES measurements with 21.2-eV photons. **g–i**, Schematics for the sign of the S_x, S_y and S_z polarization in the three-dimensional Brillouin zone, showing plaid-like antisymmetric spin texture across the high-symmetry planes. **j**, DFT-calculated spin-resolved bands without SOC. There is no in-plane spin polarization in the $k_z = 0$ (Γ–X–M–X1) plane, whereas a high level of spin polarization is seen in the O–A–B–C plane. **k**,**l**, DFT-calculated spin-resolved CEC at $k_z = \pm 0.2\pi/c$ and at binding energy $E_B = 0.45$ eV. Magenta arrows, in-plane direction of the spin; darkness of arrows, magnitude of in-plane spin polarization; colour of bands, magnitude of the out-of-plane S_z polarization. Clearly, S_α is antisymmetric about the $k_\beta = 0$ and $k_\gamma = 0$ planes and symmetric about the $k_\alpha = 0$ plane ($\alpha, \beta, \gamma = x, y, z$).

the three-dimensional Brillouin zone, consistent with our calculations. Temperature-dependent SARPES measurements further indicate that the observed spin polarization is related to the AFM to paramagnetic transition. Our work uncovers a quadratic spin-splitting effect induced by magnetic exchange, distinct from the well-known Zeeman, Rashba and Dresselhaus scenarios, in terms of the spin texture as well as the underlying mechanism (Extended Data Table 1).

Calculated spin polarization in $MnTe_2$

We begin with the essential physical properties of the $MnTe_2$ single crystals (see Methods and Extended Data Fig. 1 for details). It is interesting and rare that the crystalline space group, the magnetic space group and the spin space group of $MnTe_2$, shown in Fig. 1e, are the same (Pa-3), indicating that the noncoplanar AFM order and SOC do not break any spatial symmetries. Because of these groups, $MnTe_2$ has neither PT (spatial inversion followed by time reversal) nor $U\tau_{1/2}$ (unitary spin inversion followed by fractional translation) symmetry, satisfying the design principle of the momentum-dependent spin splitting purely induced by the AFM order[4,6].

Figure 1f shows the first Brillouin zone of $MnTe_2$, in which we mark the high-symmetry plane Γ–X1–M–X and the ARPES-measured, parallel O–A–B–C plane with $k_z = -0.2\pi/c$ (see Extended Data Fig. 2 for the discussion of k_z dispersion). Figure 1g–i are schematics of the S_x, S_y and S_z components of the valence band, in which the blue and red plaids represent the positive and negative spin polarization component, respectively. The spin-resolved E–k dispersion and constant-energy contours (CECs) through density functional theory (DFT) calculation, in Fig. 1j–l, reveal two main features. First, instead of SOC, the spin splitting of the itinerant electron is determined by the inhomogeneous magnetic field from the AFM order. The DFT-calculated E–k dispersion without SOC (Fig. 1j) exhibits a large spin splitting for the O–A–B–C plane, with comparable magnitude to the SOC-included case (Extended Data Fig. 3a), even though tellurium is expected to have a pronounced SOC effect on the electronic structure. Second, a unique plaid-like spin texture with alternating polarizations on each side of a high-symmetry plane is predicted (Fig. 1g–i,k,l). This is because the four face-centred cubic Mn sublattices with different spin orientations are connected by three magnetic group mirror symmetries M_x, M_y and M_z. The spin component S_x is antisymmetric about the $k_y = 0$ plane and the $k_z = 0$ plane but symmetric about the $k_x = 0$ plane, owing to M_y ($S_x \Rightarrow -S_x, S_y \Rightarrow S_y, S_z \Rightarrow -S_z$) and M_z ($S_x \Rightarrow -S_x, S_y \Rightarrow -S_y, S_z \Rightarrow S_z$), whereas the other two components S_y and S_z have analogous transformations. The high-symmetry Γ–X1–M–X plane ($k_z = 0$) manifest no in-plane spin splitting because M_z forbids in-plane spin components (Extended Data Table 2). Therefore, we choose the O–A–B–C plane for the SARPES measurements.

Spin polarization at a fixed k_z

We next investigate the spin-polarized bands of $MnTe_2$ with systematic SARPES measurements in its AFM phase ($T = 30$ K). In the dataset of Fig. 2, photoelectrons for both spin-resolved and spin-integrated measurements were excited by a He lamp with $h\nu = 21.2$ eV. This photon energy is found to correspond to $k_z = -0.2\pi/c$, that is, the O–A–B–C plane in Fig. 1f. The bands observed by ARPES are bulk electronic states with substantial k_z broadening (see Methods and Extended Data Figs. 2 and 4 for more discussion). As illustrated in Fig. 2b, the measured CEC has the shape of a cross with arms along the O–A and O–C directions, consistent with the DFT-calculated bulk bands (Fig. 2c,d). It is clear that the DFT bulk bands are highly spin polarized, with in-plane polarization vectors S_x (S_y) antisymmetric about the O–A (O–C) line. Such

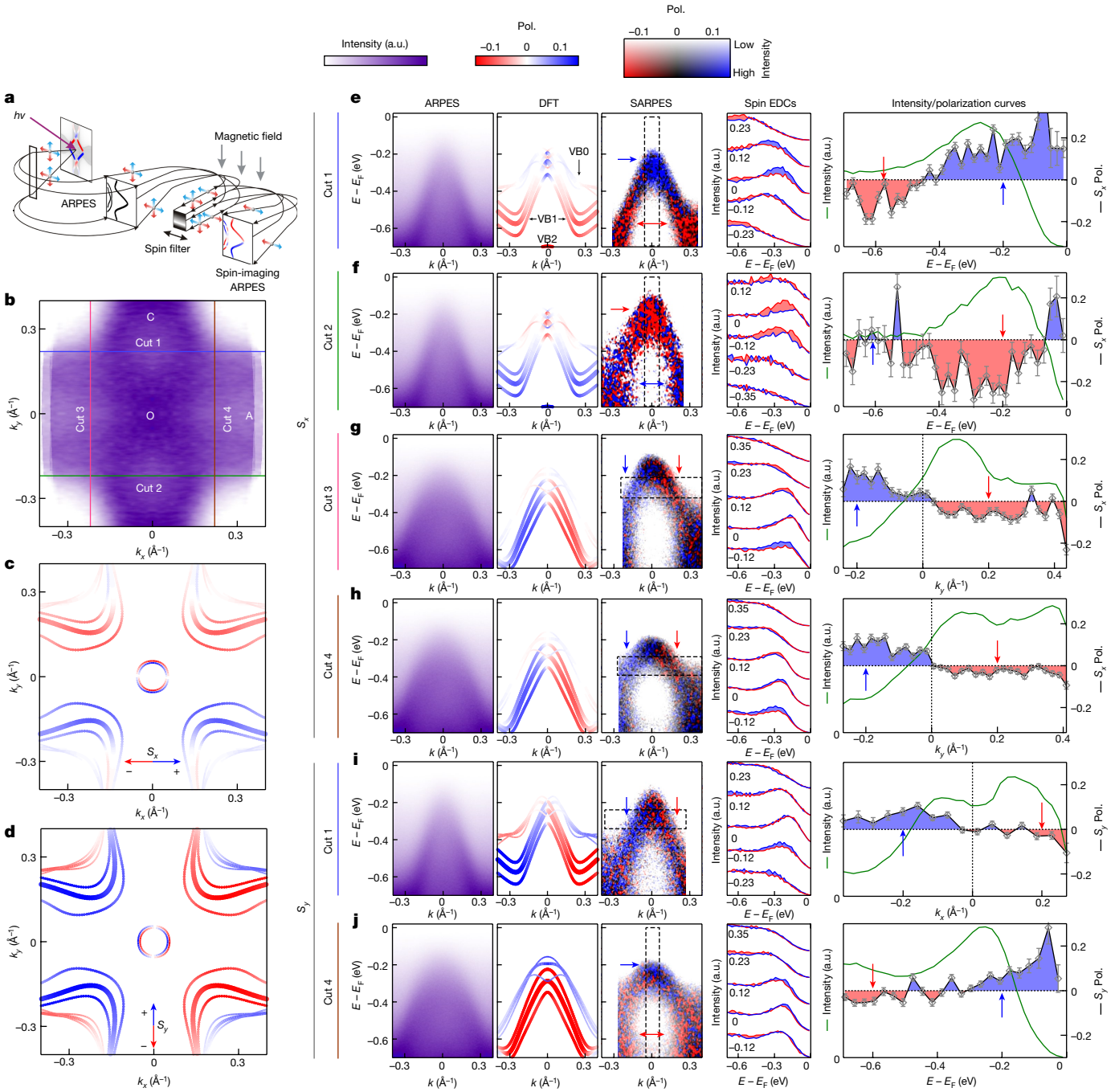

Fig. 2 | Plaid-like texture of in-plane spins at $k_z = -0.2\pi/c$. a, Schematic setup of the spin-imaging ARPES system (see Methods). **b**, ARPES-derived, spin-integrated CEC at binding energy $E_B = 0.45$ eV. **c**,**d**, Corresponding DFT-calculated, S_x-resolved and S_y-resolved CECs of bulk electronic states. The k_z-broadening effect is considered by plotting the calculated CECs at $k_z = -0.1, -0.2$ (widened) and $-0.3\pi/c$ together. Blue (red) colour represents the level of S_x+ (S_x−)/S_y+ (S_y−) polarization (same below). **e**–**j**, From left to right: spin-integrated ARPES band dispersion; DFT-calculated bulk bands; SARPES band dispersion; spin-resolved EDCs; and spin-integrated ARPES intensity (green curve), as well as spin polarization (symbols and solid black curve) versus binding energy or momentum. SARPES band dispersion is multiplied by the total intensity ($I_{up} + I_{down}$) for better visualization of spin polarization on the bands. Red and blue arrows highlight the signs of the spin. The k positions of spin-resolved EDCs are marked near the curve. Each point on a curve is an integrated intensity over a (E, k) range of (20 meV, 0.12 Å^{-1}). The spin-integrated ARPES intensity and spin polarization are integrated within the dashed rectangles in SARPES panels. Error bars are defined as the standard deviation of polarization within the integrated region, which reflect the deviation of polarization from the mean value. a.u., arbitrary units.

unique AFM-induced, plaid-like spin polarization is confirmed by our SARPES measurements. To see this, we present the S_x-resolved and S_y-resolved E–k images along Cuts 1–4 labelled in Fig. 2b. Each image is about ±0.22 Å^{-1} (that is, ±0.5π/a) away from O–A and O–C and thus expected to have antisymmetric in-plane spin polarization.

Figure 2e–j presents spin-integrated, DFT-calculated and SARPES band dispersion, as well as their spin-resolved energy distribution curves (EDCs) and the curves of spectral intensity and spin polarization versus binding energy and momentum, respectively. The full set of raw data for spin-resolved band dispersion is presented in Extended Data

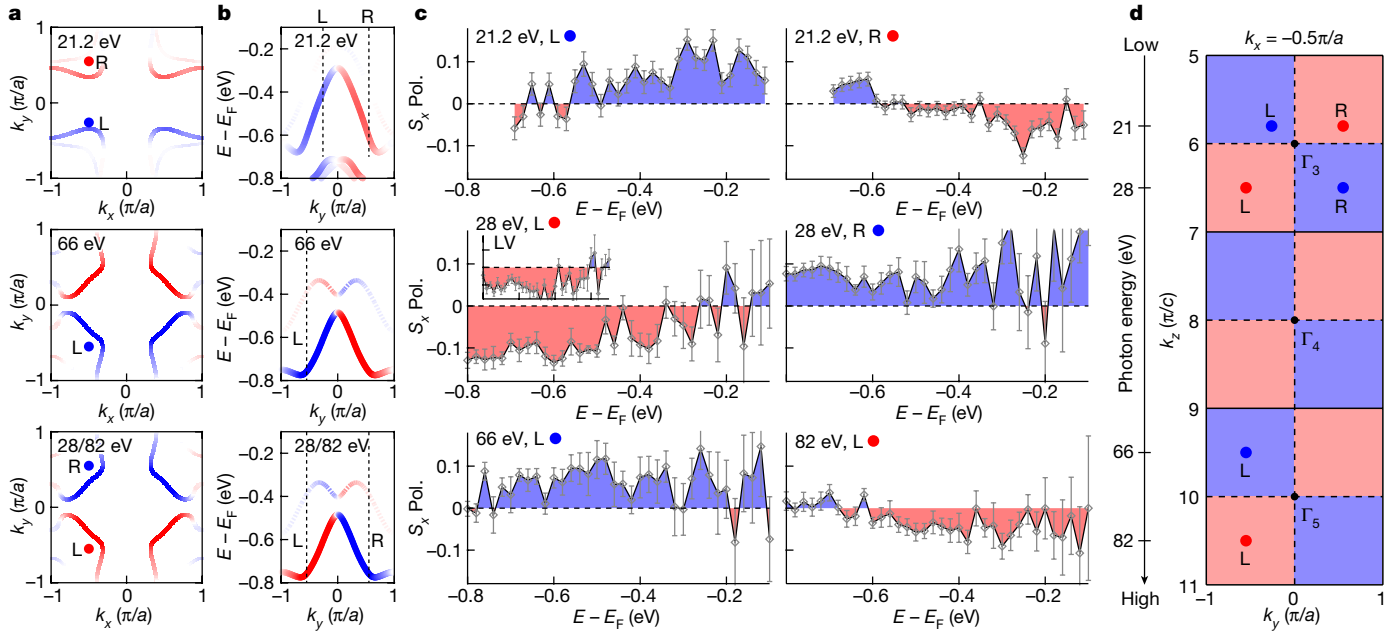

Fig. 3 | Sign reversal of the S_x polarization at different k_z values. **a**, DFT-calculated, S_x-resolved CECs at $k_z = -0.2\pi/c$ (corresponding to 21.2-eV incident photons, at binding energy $E_B = 0.45$ eV), $-0.5\pi/c$ (66 eV, $E_B = 0.65$ eV) and $0.5\pi/c$ (28 and 82 eV, $E_B = 0.65$ eV). The L and R dots mark the in-plane momenta of the polarization curves shown in **c**. **b**, DFT-derived, S_x-resolved E–k dispersion at $k_x = -0.5\pi/a$, crossing the L and R points (dashed lines). S_x is antisymmetric about the $k_y = 0$ and $k_z = 0$ planes owing to the mirror symmetries M_y and M_z. **c**, Measured S_x polarization at the L and R points, at $k_z = -0.2\pi/c$ (21.2 eV), $0.5\pi/c$ (28 eV), $-0.5\pi/c$ (66 eV) and $0.5\pi/c$ (82 eV). Incident light is LH, except for the inset of panel $0.5\pi/c$ (28 eV, L), in which it is LV. Error bars are defined the same way as in Fig. 2. S_x is found to be antisymmetric about both the $k_y = 0$ and the $k_z = 0$ planes, consistent with DFT calculations. **d**, Schematics of S_x versus k_z (that is, versus photon energy), showing the characteristic plaid-like texture.

Fig. 5. Overall, consistency between the DFT-extracted spin polarization and that measured by SARPES is reached. A closer look at the SARPES data leads to several interesting observations. First, the S_x-resolved E–k maps along Cuts 1 and 2 (shown in Fig. 2e,f) exhibit opposite S_x polarization, which is caused by the mirror reflection M_y: $S_x \Rightarrow -S_x$. Also, the S_x polarization in Cuts 1 and 2 are opposite at the top and shoulders of VB1, which is also well reproduced by DFT calculations with and without SOC (Extended Data Fig. 3). Second, for Cuts 3 and 4, the S_x polarization of VB1 is antisymmetric about $k_y = 0$ (Fig. 2g,h). Third, the situation for the spin component S_y is opposite. The measured spectra along Cuts 1 and 4 (Fig. 2i,j) exhibit a high level of S_y polarization that is antisymmetric about O–C ($k_x = 0$) owing to the mirror reflection M_x: $S_y \Rightarrow -S_y$, consistent with the DFT calculations. The same conclusions can also be drawn with the spin EDCs and polarization curves. Furthermore, the SARPES data along Cuts 5 and 6 shown in Extended Data Fig. 6 demonstrate that the in-plane spin texture is Dresselhaus-like, with substantial radial components along the diagonal directions of the in-plane Brillouin zone. On the basis of such data, we conclude that momentum-dependent antisymmetric spin splitting with plaid-like alternating spin texture exists in the noncoplanar antiferromagnet $MnTe_2$ in its magnetic ground state.

Antisymmetric spin components along k_z

After establishing the existence of the spin-polarized bands in the AFM phase of $MnTe_2$, a crucial topic is to experimentally differentiate the observed spin texture from those induced by SOC in the surface states. The characteristic sign reversal of the spin at opposite out-of-plane momenta (k_z values) would pinpoint the AFM origin of the observed polarization, as no k_z dispersive behaviour of the spin is expected in any spin-splitting effects originated from surface inversion breaking. In Fig. 3, we show such k_z-dependent sign change. We present SARPES data taken at a synchrotron-based SARPES setup at four different incident photon energies, corresponding to four different k_z values: 21.2 eV ($k_z = -0.2\pi/c$), 28 eV ($k_z = 0.5\pi/c$), 66 eV ($k_z = -0.5\pi/c$) and 82 eV ($k_z = 0.5\pi/c$). At each photon energy, polarization curves are measured at one or two k points, marked as 'L' and 'R'. According to DFT calculations on the bulk bands (Fig. 3a,b), the sign of S_x will reverse across the high-symmetry planes $k_z = 0$ and $k_y = 0$. Indeed, this is what we observed experimentally in Fig. 3c. At the L position, S_x is found to reverse sign between 21.2 eV ($S_x > 0$) and 28 eV ($S_x < 0$) and between 66 eV ($S_x > 0$) and 82 eV ($S_x < 0$); at the R position, S_x is found to reverse sign between 21.2 eV ($S_x < 0$) and 28 eV ($S_x > 0$). Across the in-plane high-symmetry plane of $k_y = 0$, S_x is also found to reverse sign between the L and R points at both 21.2 eV and 28 eV, further verifying the antisymmetric plaid-like feature within a certain k_z plane.

To eliminate the effect of possible matrix elements associated with different light polarizations, we measured the S_x polarization at the L point at $h\nu = 28$ eV under two different incident beam polarizations, linearly polarized horizontally (LH) and linearly polarized vertically (LV), which adds up to an unpolarized situation (see Methods for more discussion). Both curves give $S_x < 0$ for most of the binding energies. Therefore, we argue that the measured polarization reflects the intrinsic spin of the band. The k_z-dependent spin polarization is summarized in Fig. 3d. We mark the measured sign of S_x polarizations (colour of the dots) within a schematic k_y–k_z frame, in which the plaid-like background represents the calculated sign of S_x. The consistency consolidates that the plaid-like spin texture is also observed along the out-of-plane momentum direction.

Temperature dependence

To verify the magnetic origin of such spin splitting, another critical piece of evidence is the temperature evolution of spin polarization[42]. Temperature changes are not expected to influence the strength of relativistic SOC, which is primarily dependent on atomic mass. By contrast, for AFM-induced spin splitting, the spin polarization is expected to disappear when the system evolves to the paramagnetic state above

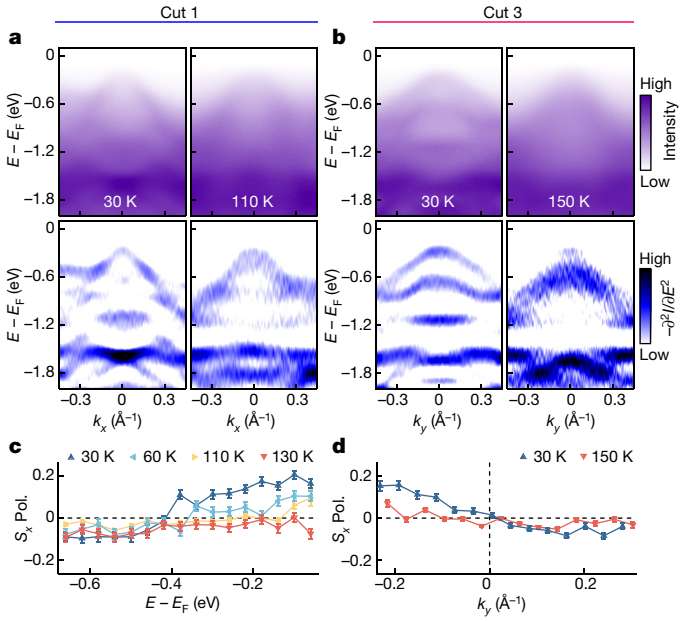

Fig. 4 | Temperature dependence of the band structure and the S_x polarization. a,**b**, Spin-integrated band dispersion along Cuts 1 and 3 below and above T_N = 87 K and corresponding second-derivative results along the EDCs. **c**,**d**, Temperature evolution of S_x. The measurement positions are the same as in Fig. 2e,g, respectively. Compared with the 30-K data, S_x decreases by about one-half at T = 60 K and nearly becomes zero for $T > T_N$. This result supports the AFM-induced spin-polarization mechanism, rather than the SOC-originated ones, which are constant at all temperatures.

the Néel temperature T_N (87 K). Our data in Fig. 4 support the latter case. Figure 4a,b shows the spin-integrated band dispersion along Cut 1 at 30 K and 110 K, as well as along Cut 3 at 30 K and 150 K. From both the raw data and the second-derivative result, we notice that the overall band structure undergoes substantial modification as temperature rises above T_N = 87 K (see Extended Data Figs. 7 and 8 for more details). Notably, such change of bands in the high-T paramagnetic phase is accompanied with an abrupt decrease of spin polarization. In Fig. 4c,d, we show the temperature-dependent S_x-polarization curves along Cuts 1 and 3. It is apparent that signatures of S_x polarization almost vanishes at high temperatures, in sharp contrast to the curves at 30 K, at which sign-changing S_x components are seen for different binding energies/in-plane momenta.

Further evidence is presented in Extended Data Fig. 9, in which we plot the evolution of spin splitting along Cut 5 across T_N, as well as SARPES E–k images along Cut 1 at 30 K and 60 K. The pair of bands along Cut 5 seemingly split in momentum like the Rashba–Dresselhaus pairs at 30 K is found to merge into a single band at 150 K (Extended Data Fig. 9a,b), evident for the vanishing of spin splitting above T_N. The same data also give an estimation of the spin-splitting energy level: about 274 ± 40 meV at $k_{||} = \pm 0.18$ Å^{-1}. This value is comparable with the largest known 'giant Rashba splitting' found in BiTeI (ref. 38). In the SARPES images (Extended Data Fig. 9c,d), the blue ($S_x > 0$) part at 30 K becomes mix coloured at 60 K, indicative of a decrease in spin polarization, whereas the overall shape and E–k location of the band itself is unchanged. Taken collectively, our data probably identify that the observed spin-splitting effect in $MnTe_2$ is induced by the AFM order.

Quadratic spin texture

Our experimental results—the sign reversal of spin across $k_z = 0$ (Fig. 3) and the decrease of polarization across T_N (Fig. 4)—serve as evidence for an AFM-induced spin splitting in $MnTe_2$. We now discuss more deeply the uniqueness of the observed plaid-like spin texture compared with the classical spin textures caused by SOC. For simplicity, we consider systems with inversion symmetry P in the bulk, such as $MnTe_2$, in which bulk Dresselhaus and Weyl spin splitting are prohibited. Thus, the SOC-induced spin splitting is associated with P breaking at the surface. Because SOC does not break time-reversal T, symmetry requirements enforce that the spin-splitting $k \cdot p$ Hamiltonian expanded at time-reversal-invariant momenta only allow odd-order k polynomials, such as linear/cubic Rashba or Dresselhaus terms. By sharp contrast, when considering AFM order as the mechanism of spin splitting, the existence of P and breaking of T results in the $k \cdot p$ Hamiltonian at time-reversal-invariant momenta points having only even-order k polynomials[43]. In the case of $MnTe_2$, the Hamiltonian expanded near the Γ point is written as $k_z(k_y\sigma_x + k_x\sigma_y)$ (see Methods for details). Such a quadratic spin texture naturally leads to the sign reversal of spin across $k_z = 0$.

Extended Data Table 1 summarizes the critical symmetries, observable characters, the nature of $k \cdot p$ Hamiltonians and spin patterns of the two distinct spin-splitting phenomena. We note that, although at $k_z > 0$ plaid-like and linear Dresselhaus spin splitting share qualitatively the same in-plane spin patterns, the k_z dependence of the former reveals the nature of an unprecedentedly measured quadratic spin texture, which is underlaid by the mechanism of time-reversal breaking.

In summary, our systematic SARPES measurements have demonstrated the existence of a new type of momentum-dependent spin splitting induced by the intrinsic AFM order in a noncoplanar antiferromagnet, $MnTe_2$. We emphasize that this type of spin splitting in noncoplanar and noncollinear antiferromagnets has the same origin as that in collinear altermagnets, as the local AFM field couples the electron spin and its motion in the same manner. The momentum-dependent spin-splitting bands in $MnTe_2$ can efficiently generate spin-polarized current, leading to magnetic spin Hall effect[44–46], spin-splitter effect, tunnelling magnetoresistance etc. Furthermore, such a spin-splitting effect could also exist in a variety of quantum materials, such as Mott insulators[47], parent compounds of unconventional superconductors[48] and three-dimensional quantum Hall materials[49,50], providing a path to study these exotic phases of matter and potential applications in spintronics.

Online content

Any methods, additional references, Nature Portfolio reporting summaries, source data, extended data, supplementary information, acknowledgements, peer review information; details of author contributions and competing interests; and statements of data and code availability are available at https://doi.org/10.1038/s41586-024-07023-w.

1. Žutić, I., Fabian, J. & Das Sarma, S. Spintronics: fundamentals and applications. *Rev. Mod. Phys.* **76**, 323–410 (2004).
2. Dieny, B. et al. Opportunities and challenges for spintronics in the microelectronics industry. *Nat. Electron.* **3**, 446–459 (2020).
3. Datta, S. & Das, B. Electronic analog of the electro-optic modulator. *Appl. Phys. Lett.* **56**, 665–667 (1990).
4. Liu, P., Li, J., Han, J., Wan, X. & Liu, Q. Spin-group symmetry in magnetic materials with negligible spin-orbit coupling. *Phys. Rev. X* **12**, 021016 (2022).
5. Pekar, S. I. & Rashba, É. I. Combined resonance in crystals in inhomogeneous magnetic fields. *Zh. Eksperim. Teor. Fiz.* **47**, 1927–1930 (1964).
6. Yuan, L. D., Wang, Z., Luo, J. W., Rashba, É. I. & Zunger, A. Giant momentum-dependent spin splitting in centrosymmetric low-Z antiferromagnets. *Phys. Rev. B* **102**, 014422 (2020).
7. Šmejkal, L., González-Hernández, R., Jungwirth, T. & Sinova, J. Crystal time-reversal symmetry breaking and spontaneous Hall effect in collinear antiferromagnets. *Sci. Adv.* **6**, eaaz8809 (2020).
8. Hayami, S., Yanagi, Y. & Kusunose, H. Momentum-dependent spin splitting by collinear antiferromagnetic ordering. *J. Phys. Soc. Jpn.* **88**, 123702 (2019).
9. Šmejkal, L., Sinova, J. & Jungwirth, T. Beyond conventional ferromagnetism and antiferromagnetism: a phase with nonrelativistic spin and crystal rotation symmetry. *Phys. Rev. X* **12**, 031042 (2022).
10. Mazin, I. I., Koepernik, K., Johannes, M. D., González-Hernández, R. & Šmejkal, L. Prediction of unconventional magnetism in doped $FeSb_2$. *Proc. Natl Acad. Sci.* **118**, e2108924118 (2021).
11. Petrovykh, D. Y. et al. Spin-dependent band structure, Fermi surface, and carrier lifetime of permalloy. *Appl. Phys. Lett.* **73**, 3459–3461 (1998).

12. Rashba, É. I. & Sheka, V. I. Symmetry of energy bands in crystals of wurtzite type II. Symmetry of bands with spin-orbit interaction included. *Fiz. Tverd. Tela: Collected Papers* **2**, 62–76 (1959).
13. Dresselhaus, G. Spin-orbit coupling effects in zinc blende structures. *Phys. Rev.* **100**, 580–586 (1955).
14. González-Hernández, R. et al. Efficient electrical spin splitter based on nonrelativistic collinear antiferromagnetism. *Phys. Rev. Lett.* **126**, 127701 (2021).
15. Bose, A. et al. Tilted spin current generated by the collinear antiferromagnet ruthenium dioxide. *Nat. Electron.* **5**, 267–274 (2022).
16. Bai, H. et al. Observation of spin splitting torque in a collinear antiferromagnet RuO_2. *Phys. Rev. Lett.* **128**, 197202 (2022).
17. Karube, S. et al. Observation of spin-splitter torque in collinear antiferromagnetic RuO_2. *Phys. Rev. Lett.* **129**, 137201 (2022).
18. Ghosh, S., Manchon, A. & Železný, J. Unconventional robust spin-transfer torque in noncollinear antiferromagnetic junctions. *Phys. Rev. Lett.* **128**, 097702 (2022).
19. Šmejkal, L., Hellenes, A. B., González-Hernández, R., Sinova, J. & Jungwirth, T. Giant and tunneling magnetoresistance in unconventional collinear antiferromagnets with nonrelativistic spin-momentum coupling. *Phys. Rev. X* **12**, 011028 (2022).
20. Shao, D. F., Zhang, S. H., Li, M., Eom, C. B. & Tsymbal, E. Y. Spin-neutral currents for spintronics. *Nat. Commun.* **12**, 7061 (2021).
21. Qin, P. et al. Room-temperature magnetoresistance in an all-antiferromagnetic tunnel junction. *Nature* **613**, 485–489 (2023).
22. Chen, X. et al. Octupole-driven magnetoresistance in an antiferromagnetic tunnel junction. *Nature* **613**, 490–495 (2023).
23. Jungwirth, T., Marti, X., Wadley, P. & Wunderlich, J. Antiferromagnetic spintronics. *Nat. Nanotechnol.* **11**, 231–241 (2016).
24. Baltz, V. et al. Antiferromagnetic spintronics. *Rev. Mod. Phys.* **90**, 015005 (2018).
25. Ren, J. et al. Enumeration and representation of spin space groups. Preprint at https://arxiv.org/abs/2307.10369 (2023).
26. Chen, X., Ren, J., Li, J., Liu, Y. & Liu, Q. Spin space group theory and unconventional magnons in collinear magnets. Preprint at https://arxiv.org/abs/2307.12366 (2023).
27. Xiao, Z., Zhao, J., Li, Y., Shindou, R. & Song, Z. D. Spin space groups: full classification and applications. Preprint at https://arxiv.org/abs/2307.10364 (2023).
28. Jiang, Y. et al. Enumeration of spin-space groups: towards a complete description of symmetries of magnetic orders. Preprint at https://arxiv.org/abs/2307.10371 (2023).
29. Brinkman, W. F. & Elliott, R. J. Theory of spin-space groups. *Proc. R. Soc. A* **294**, 343–358 (1966).
30. Litvin, D. B. & Opechowski, W. Spin groups. *Physica* **76**, 538–554 (1974).
31. Litvin, D. B. Spin point groups. *Acta Cryst. A* **33**, 279–287 (1977).
32. Yang, J., Liu, Z.-X. & Fang, C. Symmetry invariants and classes of quasi-particles in magnetically ordered systems having weak spin-orbit coupling. Preprint at https://arxiv.org/abs/2105.12738 (2021).
33. Liu, P., Zhang, A., Han, J. & Liu, Q. Chiral Dirac-like fermion in spin-orbit-free antiferromagnetic semimetals. *Innovation* **3**, 100343 (2022).
34. Zhang, A. et al. Chiral Dirac fermion in a collinear antiferromagnet. *Chin. Phys. Lett.* **40**, 126101 (2023).
35. Ma, H. Y. et al. Multifunctional antiferromagnetic materials with giant piezomagnetism and noncollinear spin current. *Nat. Commun.* **12**, 2846 (2021).
36. Feng, Z. et al. An anomalous Hall effect in altermagnetic ruthenium dioxide. *Nat. Electron.* **5**, 735–743 (2022).
37. Ghimire, N. et al. Large anomalous Hall effect in the chiral-lattice antiferromagnet $CoNb_3S_6$. *Nat. Commun.* **9**, 3280 (2018).
38. Ishizaka, I. et al. Giant Rashba-type spin splitting in bulk BiTeI. *Nat. Mater.* **10**, 521–526 (2011).
39. Šmejkal, L., Sinova, J. & Jungwirth, T. Emerging research landscape of altermagnetism. *Phys. Rev. X* **12**, 040501 (2022).
40. Ji, F. et al. Multichannel exchange-scattering spin polarimetry. *Phys. Rev. Lett.* **116**, 177601 (2016).
41. Zha, H. et al. Improvement of image-type very-low-energy-electron-diffraction spin polarimeter. *Rev. Sci. Instrum.* **94**, 073704 (2023).
42. Schrunk, B. et al. Emergence of Fermi arcs due to magnetic splitting in an antiferromagnet. *Nature* **603**, 610–615 (2022).
43. Liu, Y., Li, J., Liu, P. & Liu, Q. Universal theory of spin-momentum-orbital-site locking. Preprint at https://arxiv.org/abs/2306.16312 (2023).
44. Železný, J., Zhang, Y., Felser, C. & Yan, B. Spin-polarized current in noncollinear antiferromagnets. *Phys. Rev. Lett.* **119**, 187204 (2017).
45. Zhang, Y., Železný, J., Sun, Y., van den Brink, J. & Yan, B. Spin Hall effect emerging from a noncollinear magnetic lattice without spin–orbit coupling. *New J. Phys.* **20**, 073028 (2018).
46. Kimata, M. et al. Magnetic and magnetic inverse spin Hall effects in a non-collinear antiferromagnet. *Nature* **565**, 627–630 (2019).
47. Xu, H. C. et al. Direct observation of the bandwidth control Mott transition in the $NiS_{2-x}Se_x$ multiband system. *Phys. Rev. Lett.* **112**, 087603 (2014).
48. Damascelli, A., Hussain, Z. & Shen, Z. X. Angle-resolved photoemission studies of the cuprate superconductors. *Rev. Mod. Phys.* **75**, 473–541 (2003).
49. Shindou, R. & Nagaosa, N. Orbital ferromagnetism and anomalous Hall effect in antiferromagnets on the distorted fcc lattice. *Phys. Rev. Lett.* **87**, 116801 (2001).
50. Halperin, B. Possible states for a three-dimensional electron gas in a strong magnetic field. *Jpn. J. Appl. Phys.* **26**, 1913–1919 (1987).

Publisher's note Springer Nature remains neutral with regard to jurisdictional claims in published maps and institutional affiliations.

Springer Nature or its licensor (e.g. a society or other partner) holds exclusive rights to this article under a publishing agreement with the author(s) or other rightsholder(s); author self-archiving of the accepted manuscript version of this article is solely governed by the terms of such publishing agreement and applicable law.

© The Author(s), under exclusive licence to Springer Nature Limited 2024

Methods

Sample growth and characterization

Single crystals of $MnTe_2$ were synthesized by the chemical vapour transport method. Manganese powder, tellurium powder and iodine crystals were mixed and sealed into a silica tube under vacuum. After heating at 600 °C with a temperature gradient of 60 °C for 10 days, millimetre-size plate-shaped $MnTe_2$ single crystals were obtained, shown in Extended Data Fig. 1a.

$MnTe_2$ samples were characterized by X-ray diffraction using a Rigaku SmartLab diffractometer with Cu Kα radiation at room temperature. The diffraction pattern in Extended Data Fig. 1a confirms the pyrite structure in the space group *Pa*-3, in which the cleaving planes are parallel to the (001) crystallographic orientation. In the lattice, manganese and tellurium atoms are located at the 4a and 8c Wyckoff positions, respectively. The crystal is composed of face-centred cubic Mn sublattices connected by $MnTe_6$ octahedra.

In Extended Data Fig. 1b, the magnetic properties were measured by a Quantum Design Physical Property Measurement System with a magnetic field up to 7 T. The temperature dependence of the magnetization curve indicates that the Néel temperature is about 87 K, consistent with previous studies[51,52]. Residual magnetization below 87 K is seen in our field-cooled (FC) *M*–*T* curve, whereas an abrupt downturn of magnetization at 87 K is seen in our zero-field-cooled (ZFC) *M*–*T* curve. This signifies an AFM behaviour at low temperatures. The magnetic field dependence of the magnetization curve is linear, indicating that no ferromagnetism is observed in our measurements.

Extended Data Fig. 1c,d presents a scanning electron microscopy image with corresponding energy-dispersive X-ray spectroscopy elemental maps, measured with a ZEISS MERLIN scanning electron microscope setup at the SUSTech Core Research Facilities. The uniform colour of the maps indicates a homogeneous distribution of the Mn and Te elements. Extended Data Fig. 1d shows further that the atomic ratio of Mn:Te is close to 1:2 on all areas measured. Small but systematic deviation to the stoichiometric value implies slight but uniform Te deficiency in the crystal, leading to a refined chemical composition $MnTe_{2-\delta}$, with $\delta \approx 0.18$. On the basis of these data, we deduce that the crystals we used are of high quality and single phased.

Lab-based spin-integrated ARPES measurements

Lab-based spin-integrated ARPES measurements were performed at Westlake University with a Scienta Omicron DA30 electron analyser using a He lamp with $h\nu = 21.2$ eV as the light source. The $MnTe_2$ samples were cleaved in situ and measured in an ultrahigh vacuum with a base pressure better than 1.5×10^{-10} mbar. Angular and energy resolutions were set to 0.1° and 5 meV, respectively.

In Fig. 2b, the measured CEC shows two different arms along the O–A and O–C directions, respectively. The arm along O–A is found to be slightly 'wider' than that along O–C, as there is no C_4 symmetry in this system, despite its cubic crystal structure. Such subtle difference not only guides us to align the samples and determine the spin directions during the experiment but also infers that the magnetic domains in the $MnTe_2$ crystals have one preferred orientation over the others. To confirm this, we performed both scanning nitrogen-vacancy (NV) magnetometry measurements as well as SARPES experiments before and after a 90° rotation of the sample. Results from both techniques (Extended Data Fig. 10) are supportive for a domain size comparable with the incident beam spot, or a preferable orientation of magnetic moments within the region of the incident beam.

Spin-integrated ARPES band dispersion along Cuts 1–4 (Fig. 2e–j) exhibit a single hole-like band near E_F, consistent with the calculation results that the main hole-like band (VB1) coexists with another band (VB0) at lower binding energies (see also Extended Data Fig. 3). Although this extra band is almost invisible in Fig. 2, its ARPES intensity and associated spin polarization is found to be present along Cuts 5 and 6, which are 45° rotated with respect to Cuts 1–4 (Extended Data Fig. 6). Considering its reduced ARPES and SARPES signal (probably because of the matrix-element effect), we lower the spin signal of VB0 by one-half on every theoretical *E*–*k* cut throughout the paper.

Synchrotron-based spin-integrated ARPES measurements

The k_z dispersion data and the spin-integrated electronic structure at different photon energies in Extended Data Figs. 2 and 4 were performed at BL03U (ref. 53) of the Shanghai Synchrotron Radiation Facility (SSRF) and BL09A of the Hiroshima Synchrotron Radiation Center (HiSOR). Data at BL03U of the SSRF are measured with a Scienta Omicron DA30 electron analyser and *p*-polarized light with photon energies between 50 and 160 eV. The sample was cleaved in situ with a base pressure of 9×10^{-11} mbar. Data at BL09A of the HiSOR are measured with a SPECS PHOIBOS 150 electron analyser and *p*-polarized light with photon energies between 11 and 40 eV. The sample was cleaved in situ with a base pressure of 1×10^{-10} mbar. The measurement temperature is 30 K for both facilities.

In Extended Data Figs. 2 and 4, an inner potential of $V_0 = 10$ eV is determined by comparing the experimental results with the DFT calculation results. The observed bands are seen to exhibit clear k_z dispersive behaviour, which is not present in surface states. Moreover, we show in Extended Data Fig. 11 the DFT-calculated electronic structures from a semi-infinite slab model on two possible surface terminations, differentiating bulk bands from surface states. It is found that the surface bands contribute negligibly to the spectral weight in the *E*–*k* regions we measured, endorsing the bulk nature of the observed bands in Fig. 2. Slight deviation between DFT results and the experimental data can be attributed to the k_z broadening effect of the bulk states[54], which is considered in all theoretical panels in Fig. 2 by simultaneously plotting the DFT bulk bands for neighbouring k_z values.

Lab-based SARPES measurements and data analysis

Lab-based spin-resolved electronic structures were obtained through a multichannel very-low-energy electron diffraction (VLEED) spin polarimeter attached to a Scienta R3000 hemispherical analyser at the Shanghai Institute of Microsystem and Information Technology (SIMIT), the schematics of which is shown in Fig. 2a. A multichannel SARPES *E*–*k* cut is obtained by guiding the ARPES photoelectrons through a VLEED-type spin-filtering crystal, which is pre-magnetized along the ±*x* (horizontal) or ±*y* (vertical) directions. The reflected electrons are then recorded on the charge-coupled device camera. S_x-resolved (S_y-resolved) ARPES data are obtained by subtracting the S_x+-magnetized (S_y+-magnetized) *E*–*k* map with the S_x−-magnetized (S_y−-magnetized) one[40,41]. Photoelectrons were excited by the He Iα line with $h\nu = 21.2$ eV. The sample was cleaved in situ with a base pressure of 1×10^{-10} mbar. Angular and energy resolutions were better than 0.5° and approximately 20 meV, respectively. The normal of the sample surface is parallel to the axis of the electron analyser's lens and the incidence angle of light is 60° relative to the lens axis[55]. The band-dispersion image on the exit plane of the R3000 analyser was turned around for 180° by a homogeneous magnetic field to scatter with a ferromagnetic Fe(001)-*p*(1×1)-O target and then turned around for another 180° to obtain a spin-resolved *E*–*k* image at a fluorescence screen.

The spin-resolved *E*–*k* images in Fig. 2e–j and Extended Data Figs. 9c(i),d(i) and 12 are multiplied by the total intensity ($I_{tot} = I_{mag\,up} + I_{mag\,down}$) for better visualization of spin polarization on the energy bands, in which $I_{mag\,up}$ ($I_{mag\,down}$) is the photoelectron intensity measured under opposite ferromagnetic target magnetization, whereas those in Extended Data Figs. 5, 6 and 9c(ii),d(ii) are raw SARPES *E*–*k* images, in which the intensity in each pixel is the unaltered result of $\text{Pol.} = (1/S_{eff}) \times (I_{mag\,up} - I_{mag\,down})/(I_{mag\,up} + I_{mag\,down})$, in which $S_{eff} = 0.32$ is the Sherman function. Values in the polarization curves in Fig. 2 were also defined as $\text{Pol.} = (1/S_{eff}) \times (I_{mag\,up} - I_{mag\,down})/(I_{mag\,up} + I_{mag\,down})$. The intensity

of spin-up (spin-down) photoelectrons (I_{up}/I_{down}) in Fig. 2 is calculated through $I_{up} = (1 + \text{Pol.}) \times I_{tot}/2$ and $I_{down} = (1 - \text{Pol.}) \times I_{tot}/2$.

The spin-polarized images were obtained by iterating through several loops (L1–L20), in an integration time of about 14 h. In Extended Data Fig. 13a–d, we found that the sample is slightly hole doped and the energy bands move rigidly upward to the Fermi level during the measurement process, which results in an inaccurate spin-polarization value close to E_F. To eliminate the artefact caused by hole doping, an energy-offset procedure was performed referring to the first loop (L1) in Extended Data Fig. 13b,d. It should be emphasized that the energy offset has a negligible effect on the spin polarization for $E_B > 0.1$ eV, by comparing the results with or without it (Extended Data Fig. 13e).

Data on several samples show consistent SARPES E–k images, confirming the repeatability of our measurements (Extended Data Fig. 12).

Synchrotron-based SARPES measurements and data analysis

Polarization curves (in Fig. 3c) are measured at BL09U (Dreamline) of the SSRF with a Scienta Omicron DA30 analyser and a single VLEED spin detector. The entrance slit is perpendicular to the ground and the spin direction measured by the VLEED detector is perpendicular to the slit. The measurement temperature is 30 K. The sample was cleaved in situ in an ultrahigh vacuum chamber with pressure better than 6×10^{-11} mbar. The energy resolution was set to 20 meV and the spot size of the light was 20 × 30 μm. Incident light is linearly polarized. The LH/LV (p-/s-) polarized light is defined as the electric vector of the light being parallel (perpendicular) to the plane formed by the incident direction of the light and the normal direction of the sample. S_x-polarization curves at $h\nu$ = 28, 66 and 82 eV were obtained from the same sample.

The experimental results measured using different light polarizations and photon energies can eliminate the influence of possible matrix elements[56,57]. On the one hand, the data at 21.2 eV is taken with a helium lamp, which emits essentially unpolarized light. Therefore, the matrix-element effect owing to light polarization is eliminated. On the other hand, S_x-polarization curves at the L point at $h\nu$ = 28 eV under LH and LV polarization reveal the same trend of spin polarization: $S_x < 0$ for the most part of the curves. Moreover, because 21.2-eV and 28-eV light probe the same out-of-plane Brillouin zone (centred at Γ_3), whereas 66-eV and 82-eV light probe another zone centred at Γ_5, possible matrix-element effect owing to different SARPES responses on different Brillouin zones is also eliminated. Therefore, we believe that the apparent spin polarization reflects the intrinsic spin of the band.

It should be noted here that quantitative deviations to the overall trend do occur at some of the S_x-polarization curves in Fig. 3, but this is understandable as different bands would response slightly differently under different photon energies, and the data suffer from relatively low signal-to-noise ratio, as the intrinsic spin signal is weak. Notably, a qualitative agreement is met between the theoretical three-dimensional spin texture and the measured S_x polarization.

Scanning NV magnetometry measurements

The scanning NV magnetometry[58–60] is applied to visualize the local magnetic field from the single-crystal $MnTe_2$. At the facility at the University of Stuttgart, the NV centre is implanted in the apex of a pillar etched from a diamond cantilever and is attached to the tuning fork of an atomic force microscope provided by QZabre. The NV spin state is detected through the optical excitation at 532 nm with the power of about 100 μW, so that the local magnetic field is extracted on the basis of the shift in the optically detected magnetic resonance (ODMR). To efficiently apply the microwave to the NV centre, we use copper wire with a diameter 20 μm on the top of the single-crystal $MnTe_2$, as shown in Extended Data Fig. 10a. The sample is characterized by a high spatial resolution (roughly 30 nm), which is only limited by the separation distance between the NV centre and the surface of the crystal. We have scanned over a larger scan area (50 μm) to confirm whether there are any local magnetization features presented in the surface stray field. All of the magnetometry measurements were conducted at a temperature of 2 K, far below the Néel temperature of $MnTe_2$ and with a remnant bias field of 6 Gauss along the NV axis to split the spin−1 states, which will not influence any magnetization domain of the $MnTe_2$. All two-dimensional magnetic field images are obtained by using a pulsed ODMR scheme, which can potentially reach the field sensitivity threshold of 2 $\mu T/\sqrt{Hz}$.

DFT calculations

All DFT calculations with and without SOC were performed within the Perdew–Burke–Ernzerhof[61] exchange-correlation functional using a plane-wave basis set and projector augmented-wave method[62], as implemented in the Vienna Ab initio Simulation Package (VASP)[63,64]. The experimental lattice constant of 6.90 Å, a Monkhorst–Pack (9 × 9 × 9) k-point mesh[65] and an energy cutoff of 500 eV have been used. The standard Perdew–Burke–Ernzerhof pseudopotential is adopted in all calculations, treating 13 valence electrons for Mn ($3p^6 3d^5 4s^2$) and six valence electrons for Te ($5s^2 5p^4$). To account for the correlation effects of the Mn 3d electrons, the rotationally invariant Dudarev's formalism was performed with the reported U = 5.0 and J = 0.8 eV (refs. 66,67). Atomic positions were optimized until the Hellmann–Feynman force on each atom was smaller than 0.01 eV $Å^{-1}$ and the electronic iteration was performed until the total energy change was smaller than 10^{-6} eV. The spin-projected band structures are analysed using the PyProcar code[68].

To calculate the surface states, we constructed the Wannier tight-binding Hamiltonian obtained from the Wannier90 code[69–71]. In the tight-binding Hamiltonian construction, 88 Wannier functions, including the Mn-d and Te-p orbitals, were chosen. Finally, the surface states E–k images, CECs and surface spin polarization were calculated using the retarded Green's function of semi-infinite models of $MnTe_2$. The Wannier interpolation approach with 501 × 501 (501) crystal momentum points was adopted in WannierTools[72] for calculations of CECs (E–k images).

$k \cdot p$ model

To theoretically identify the spin texture in $MnTe_2$, we constructed the $k \cdot p$ Hamiltonian near the Γ point according to the magnetic point group (little co-group) symmetries. The little co-group of the Γ point in $MnTe_2$ bulk is m-3, which contains space-inversion symmetry but breaks time-reversal symmetry. The representation matrices of the generators of m-3 with the spin basis ($|\uparrow\rangle$, $|\downarrow\rangle$) were written as:

$$A^{\Gamma}(3^{+}_{111}) = e^{-i\pi/3(\sigma_x+\sigma_y+\sigma_z)/\sqrt{3}}$$

$$A^{\Gamma}(2_{100}) = -i\sigma_x$$

$$A^{\Gamma}(2_{001}) = -i\sigma_z$$

$$A^{\Gamma}(\bar{1}) = \sigma_0,$$

in which σ_i denote the Pauli matrices. Through the theory of invariants $A^{\Gamma}(g)H^{\Gamma}(\mathbf{k})A^{\Gamma}(g)^{-1} = H^{\Gamma}(g\mathbf{k})$, the Hamiltonian near the Γ point can be obtained:

$$H^{\Gamma} = h_1\sigma_0 + h_3(k_x^2 + k_y^2 + k_z^2)\sigma_0 + h_3(k_y k_z \sigma_x + k_z k_x \sigma_y + k_x k_y \sigma_z) + O(\mathbf{k}^3)$$

in which h_i are the undetermined coefficients. To directly show the in-plane spin texture, the out-of-plane spin polarization terms and spin-independent terms could be omitted:

$$H^{\Gamma}_{in} = h_3 k_z (k_y\sigma_x + k_x\sigma_y) + O(\mathbf{k}^3).$$

Similarly, the Hamiltonian expanded near the M point (little co-group mmm) has the form $H^{M}_{in} = h_4 k_z k_y \sigma_x + h_5 k_z k_x \sigma_y + O(\mathbf{k}^3)$. Therefore, the

AFM-induced spin splitting of $MnTe_2$ bulk manifests a quadratic spin texture relative to the k polynomial.

In the case of spin splitting solely induced by SOC, a nonmagnetic symmetry group that preserves time-reversal symmetry should be used to avoid the contribution of the local moments. In this case, the bulk material exhibits both time-reversal and space-inversion symmetries, resulting in the absence of spin splitting. Therefore, spin splitting induced by SOC can only arise from the inversion symmetry breaking at the surface. The corresponding surface little co-group in $MnTe_2$ is $m1'$ and the corresponding representation matrices are expressed as:

$$A^{\Gamma}(m_{100}) = -\mathrm{i}\sigma_x,$$

$$A^{\Gamma}(T) = -\mathrm{i}\sigma_y\kappa,$$

in which κ is the conjugate operator. The corresponding Hamiltonian is written as:

$$H^{\Gamma} = h_1\sigma_0 + h_2(k_y\sigma_x - k_x\sigma_y) + h_3(k_y\sigma_x + k_x\sigma_y) + h_4k_x\sigma_z + h_5k_x^2\sigma_0 + h_6k_y^2\sigma_0 + O(\mathbf{k}^3).$$

By retaining the in-plane spin-polarization terms, the Hamiltonian now reads:

$$H_{\mathrm{in}}^{\Gamma} = h_2(k_y\sigma_x - k_x\sigma_y) + h_3(k_y\sigma_x + k_x\sigma_y) + O(\mathbf{k}^3),$$

which includes only linear Rashba and Dresselhaus terms.

Data availability

The data that support the findings of this study are available from the corresponding authors on request. Correspondence and requests of ARPES and DFT data are addressed to C.L. and those of the NV magnetometry data are addressed to J.W.

51. Hastings, J. M., Elliott, N. & Corliss, L. M. Antiferromagnetic structures of MnS_2, $MnSe_2$, and $MnTe_2$. *Phys. Rev.* **115**, 13–17 (1959).
52. Burlet, P. et al. Noncollinear magnetic structure of $MnTe_2$. *Phys. Rev. B* **56**, 14013 (1997).
53. Yang, Y. C. et al. High-resolution ARPES endstation for in situ electronic structure investigations at SSRF. *Nucl. Sci. Tech.* **32**, 31 (2021).
54. Mitsuhashi, T. et al. Influence of k broadening on ARPES spectra of the (110) and (001) surfaces of $SrVO_3$ films. *Phys. Rev. B* **94**, 125148 (2016).
55. Liu, W. J. et al. Multiple surface resonance electronic spin states in the strong topological metal Zr_2Te_2P. *Phys. Rev. B* **106**, 245144 (2022).
56. Seibel, C. et al. Photoelectron spin polarization in the Bi_2Te_3(0001) topological insulator: initial- and final-state effects in the photoemission process. *Phys. Rev. B* **93**, 245150 (2016).
57. Bentmann, H. et al. Strong linear dichroism in spin-polarized photoemission from spin-orbit-coupled surface states. *Phys. Rev. Lett.* **119**, 106401 (2017).
58. Hedrich, N. et al. Nanoscale mechanics of antiferromagnetic domain walls. *Nat. Phys.* **17**, 574–577 (2021).
59. Casola, F., van der Sar, T. & Yacoby, A. Probing condensed matter physics with magnetometry based on nitrogen-vacancy centres in diamond. *Nat. Rev. Mat.* **3**, 17088 (2018).
60. Levine, E. V. et al. Principles and techniques of the quantum diamond microscope. *Nanophotonics* **8**, 1945–1973 (2019).
61. Perdew, J. P., Burke, K. & Ernzerhof, M. Generalized gradient approximation made simple. *Phys. Rev. Lett.* **77**, 3865 (1996).
62. Blöchl, P. E. Projector augmented-wave method. *Phys. Rev. B* **50**, 17953 (1994).
63. Kresse, G. & Furthmüller, J. Efficient iterative schemes for ab initio total-energy calculations using a plane-wave basis set. *Phys. Rev. B* **54**, 11169 (1996).
64. Kresse, G. & Joubert, D. From ultrasoft pseudopotentials to the projector augmented-wave method. *Phys. Rev. B* **59**, 1758 (1999).
65. Monkhorst, H. J. & Park, J. D. Special points for Brillouin-zone integrations. *Phys. Rev. B* **13**, 5188 (1976).
66. Anisimov, V. I., Zaanen, J. & Andersen, O. K. Band theory and Mott insulators: Hubbard U instead of Stoner I. *Phys. Rev. B* **44**, 943 (1991).
67. Dudarev, S. L., Botton, G. A., Savrasov, S. Y., Humphreys, C. J. & Sutton, A. P. Electron-energy-loss spectra and the structural stability of nickel oxide: an LSDA+U study. *Phys. Rev. B* **57**, 1505 (1998).
68. Herath, U. et al. PyProcar: a Python library for electronic structure pre/post-processing. *Comput. Phys. Commun.* **251**, 107080 (2020).
69. Marzari, N. & Vanderbilt, D. Maximally localized generalized Wannier functions for composite energy bands. *Phys. Rev. B* **56**, 12847 (1997).
70. Mostofi, A. A. et al. wannier90: a tool for obtaining maximally-localised Wannier functions. *Comput. Phys. Commun.* **178**, 685–699 (2008).
71. Mostofi, A. A. et al. An updated version of wannier90: a tool for obtaining maximally-localised Wannier functions. *Comput. Phys. Commun.* **185**, 2309–2310 (2014).
72. Wu, Q., Zhang, S., Song, H.-F., Troyer, M. & Soluyanov, A. A. WannierTools: an open-source software package for novel topological materials. *Comput. Phys. Commun.* **224**, 405–416 (2018).

Acknowledgements We thank K. Miyamoto, K. Kuroda, T. Okuda, M. Zhang and L. Deng for the help in SARPES measurements, R. Peng for the help in scanning NV magnetometry measurements and J. Li for discussions. Work at SUSTech was supported by the National Key R&D Program of China (nos. 2022YFA1403700 and 2020YFA0308900), the National Natural Science Foundation of China (NSFC) (nos. 12074161 and 12274194), the Key-Area Research and Development Program of Guangdong Province (2019B010931001), the Guangdong Provincial Key Laboratory for Computational Science and Material Design (no. 2019B030301001), the Guangdong Innovative and Entrepreneurial Research Team Program (no. 2016ZT06D348) and Shenzhen Science and Technology Program (grant no. RCJC20221008092722009). The DFT calculations were performed at the Center for Computational Science and Engineering at SUSTech. Work at SIMIT was supported by the NSFC (nos. U1632266, 11927807 and U2032207) and the National Key R&D Program of China (no. 2022YFB3608000). Work at Westlake University was supported by the NSFC (no. 12274353), National Key R&D Program of China (no. 2022YFA1402200) and the Westlake Instrumentation and Service Center for Physical Sciences. D.S. acknowledges support from the NSFC (no. U2032208). C.L. acknowledges support from the Highlight Project (no. PHYS-HL-2020-1) of the College of Science, SUSTech.

Author contributions C.L. and Q.L. conceived and designed the research project. Y.-P.Z. grew and characterized the single crystals. S.Q., H.Z. and W.L. designed and built the image-type SARPES setup. Y.-P.Z., X.-R.L., H.Z., G.Q., C.H., Z.J., X.-M.M., Y.-J.H., M.-Y.Z., W.L., M.Z., J.D., S.M., K.T., M.A., Z.L., M.Y., D.S., Y.H., R.-H.H., S.Q. and C.L. performed the ARPES measurements. X.C., Y.L., P.L., J.L. and Q.L. performed the theoretical analysis and DFT calculations. S.J., M.L. and J.W. performed the scanning NV magnetometry measurements. Y.-P.Z., X.C., Q.L. and C.L. wrote the paper, with the help from all authors.

Competing interests The authors declare no competing interests.

Additional information

Supplementary information The online version contains supplementary material available at https://doi.org/10.1038/s41586-024-07023-w.

Correspondence and requests for materials should be addressed to Shan Qiao, Qihang Liu or Chang Liu.

Peer review information *Nature* thanks Ryo Noguchi and the other, anonymous, reviewer(s) for their contribution to the peer review of this work. Peer reviewer reports are available.

Reprints and permissions information is available at http://www.nature.com/reprints.

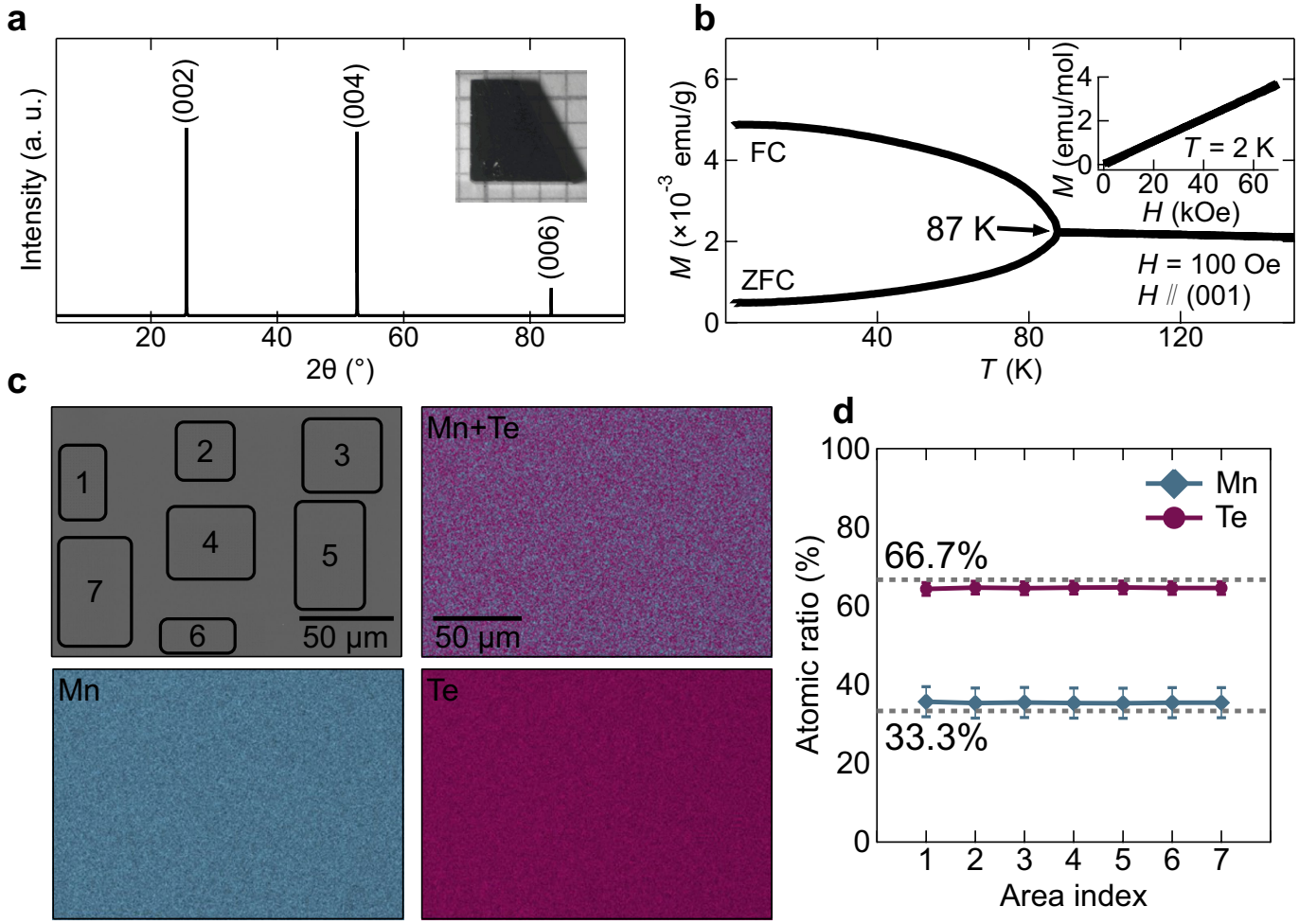

Extended Data Fig. 1 | Structural, magnetic and compositional characterization of $MnTe_2$ single crystals. a, Single-crystal X-ray diffraction results of $MnTe_2$, showing a (001) exposed plane. Inset, a $MnTe_2$ single crystal against a millimetre grid. **b**, FC and ZFC temperature dependence of magnetization with H||(001). The magnetic transition temperature is T_N = 87 K. The downturn of the ZFC M–T curve at T_N signals the AFM behaviour. Inset, magnetic-field dependence of magnetization at T = 2 K. **c**, A typical scanning electron microscopy image of the $MnTe_2$ single crystal and corresponding energy-dispersive X-ray spectroscopy elemental maps, indicating a homogeneous distribution of the Mn and Te elements. **d**, Atomic ratio of Mn and Te at the seven regions indexed in **c**. A ratio close to 1:2 is found in all regions, indicating a high quality of the crystals.

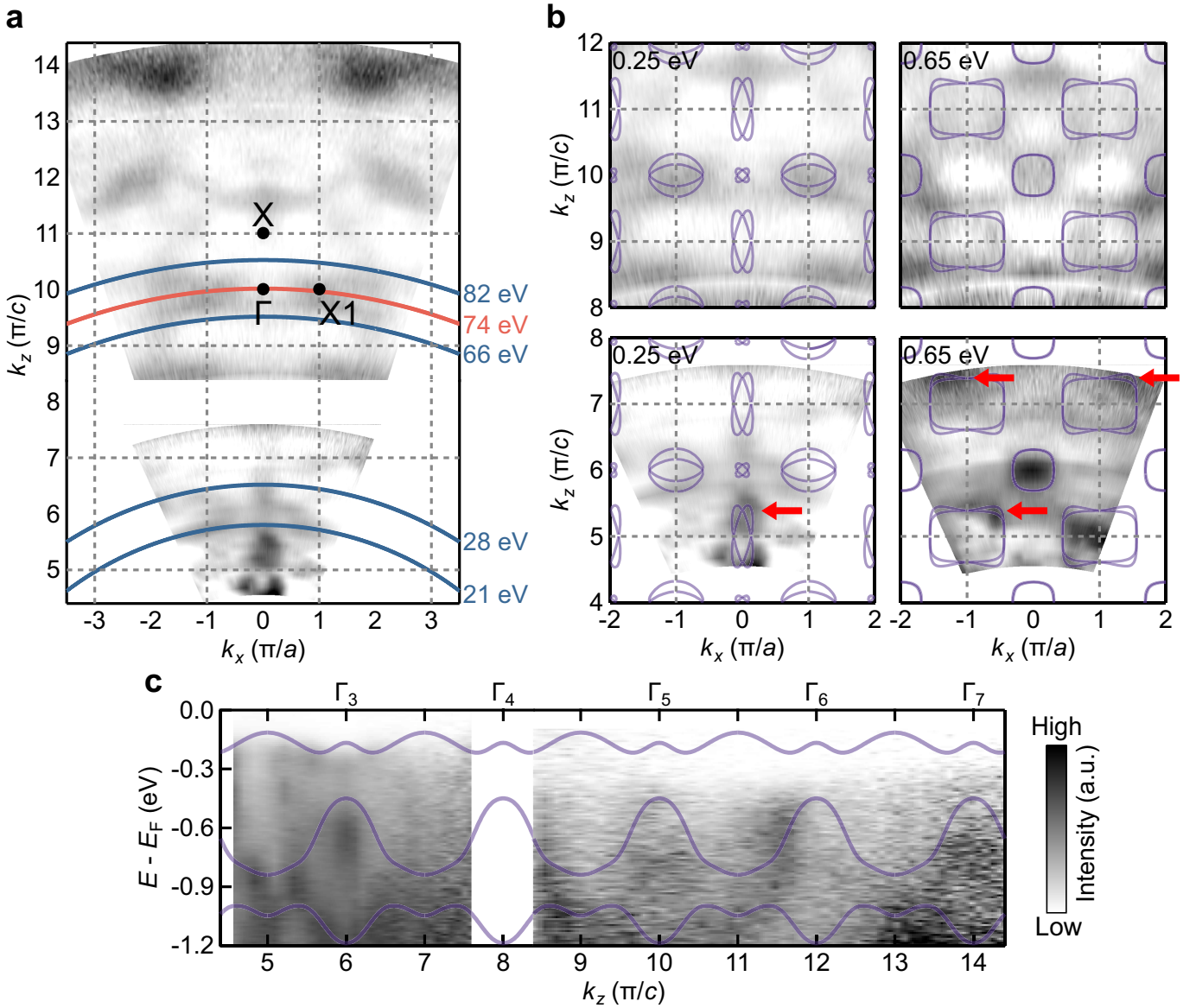

Extended Data Fig. 2 | Electronic structure along the k_x–k_z plane. a, ARPES k_x–k_z map at binding energy E_B = 0.25 eV. A clear k_z dispersion is seen, consistent with the bulk nature of the observed bands. The inner potential is determined to be V_0 = 10 eV from the data; high-symmetry points are marked accordingly. The red curve shows the k_x–k_z position of an ARPES measurement using 74-eV incident light, corresponding to $k_z = 10\pi/c$ (Γ_5) at the in-plane Brillouin zone centre. The cyan curves mark the ARPES measurement positions in Fig. 3. $h\nu$ = 21.2, 28, 66 and 82 eV correspond to k_z = 5.8 (−0.2), 6.5 (0.5), 9.5 (−0.5) and 10.5 (0.5)π/c, respectively. **b**, k_x–k_z dispersion at binding energies E_B = 0.25 and 0.65 eV, with corresponding CECs calculated by DFT. The experimental spectral intensities show rough agreement with the calculated results (indicated by red arrows). **c**, E–k_z dispersion along k_x = 0. The band at E_B = 0.5–1.0 eV is seen to experience repetitive dispersion within our measurement range, which matches qualitatively with that of a theoretical bulk band in the dispersing period, bandwidth and energy locations of band tops.

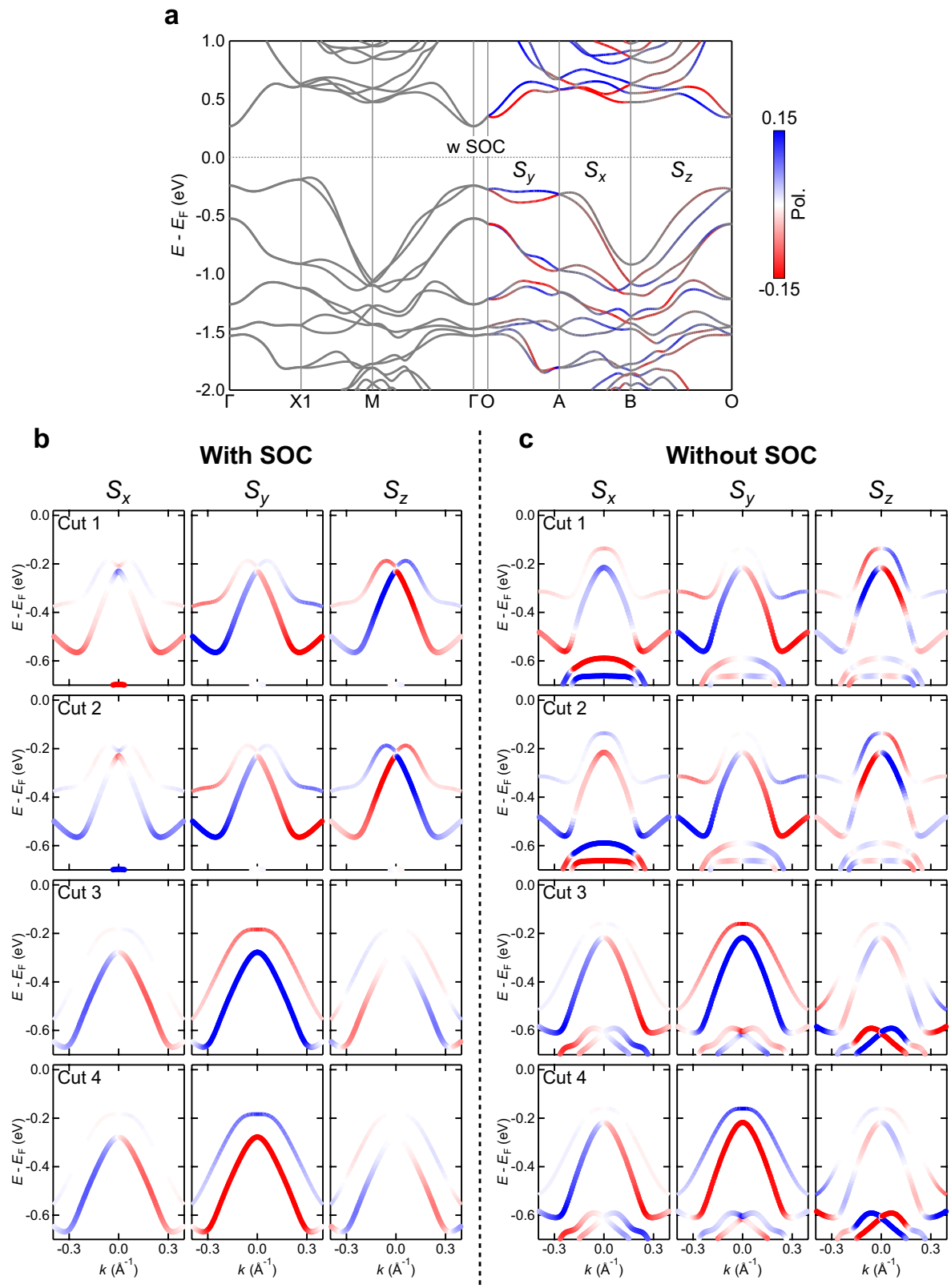

Extended Data Fig. 3 | DFT-calculated spin-resolved energy bands with and without SOC. a, *E*–*k* dispersion with SOC. A high level of spin polarization also exists in the O–A–B–C plane when SOC is turned on. A comparison between this result and Fig. 1j proves that the existence of SOC is not a necessary condition for the AFM-induced spin splitting. Even though Te is a heavy element that has strong SOC, the relativistic spin–orbit interaction gives only mild, secondary effects on the spin splitting of the $MnTe_2$ bulk bands. **b**,**c**, DFT-derived spin-resolved *E*–*k* dispersion along Cuts 1–4 with and without SOC, respectively. All calculated results show a plaid-like antisymmetric spin texture.

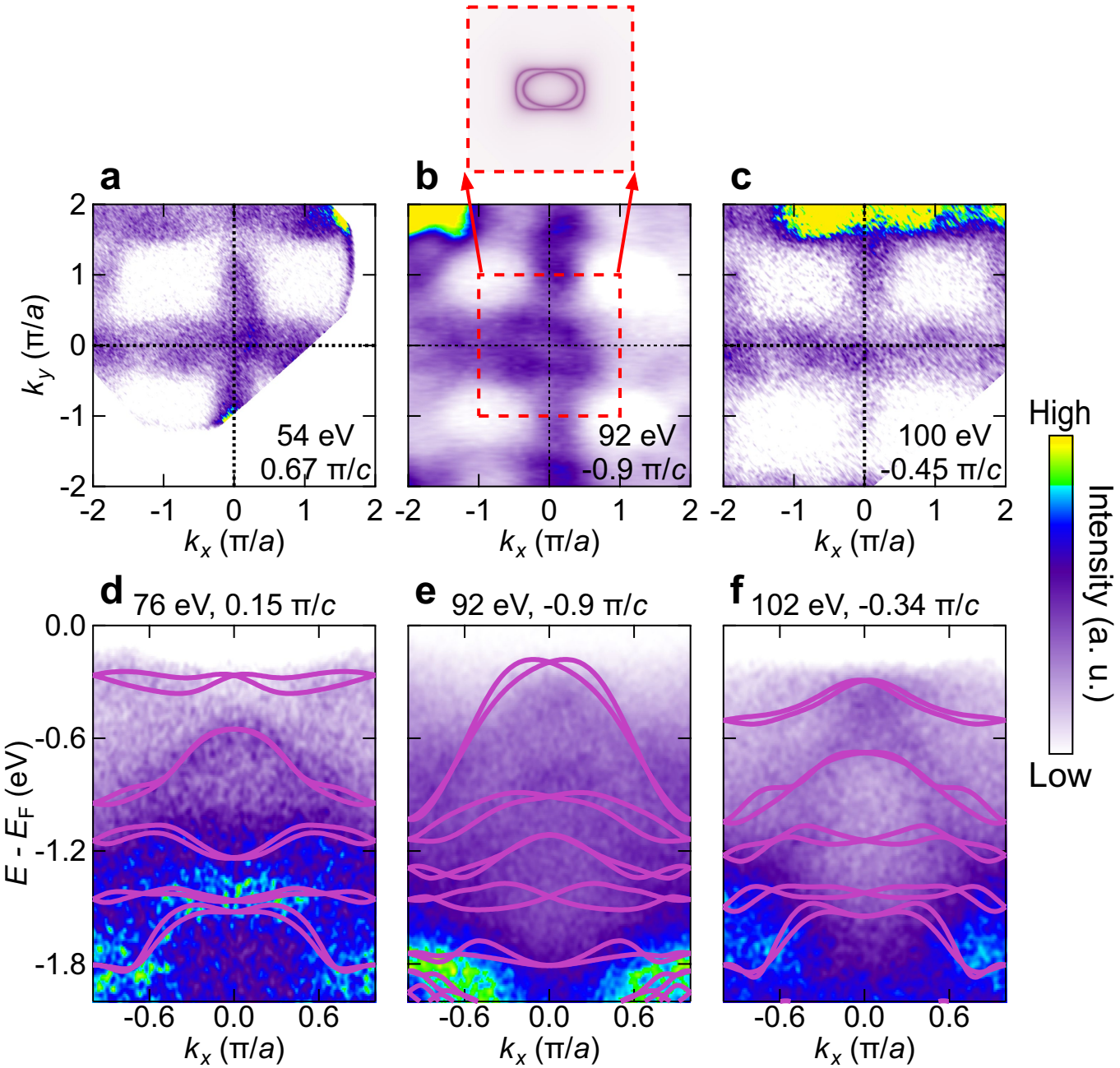

Extended Data Fig. 4 | Electronic structure at different photon energies. **a**–**c**, CECs at binding energy E_B = 0.35 eV measured with 54-eV, 92-eV and 100-eV photons. The CEC at 92 eV show a rectangular feature close to the zone centre (in good agreement with the DFT result shown in the inset), whereas the other two maps show a cross shape in the first zone. This k_z dispersive behaviour indicates the bulk nature of the bands. **d**–**f**, ARPES E–k dispersion taken with 76-eV, 92-eV and 102-eV photons. Purple curves are the bulk bands calculated by DFT. The qualitative match between the DFT bands and the ARPES data probably indicates that the ARPES intensity comes mostly from bulk states of the system.

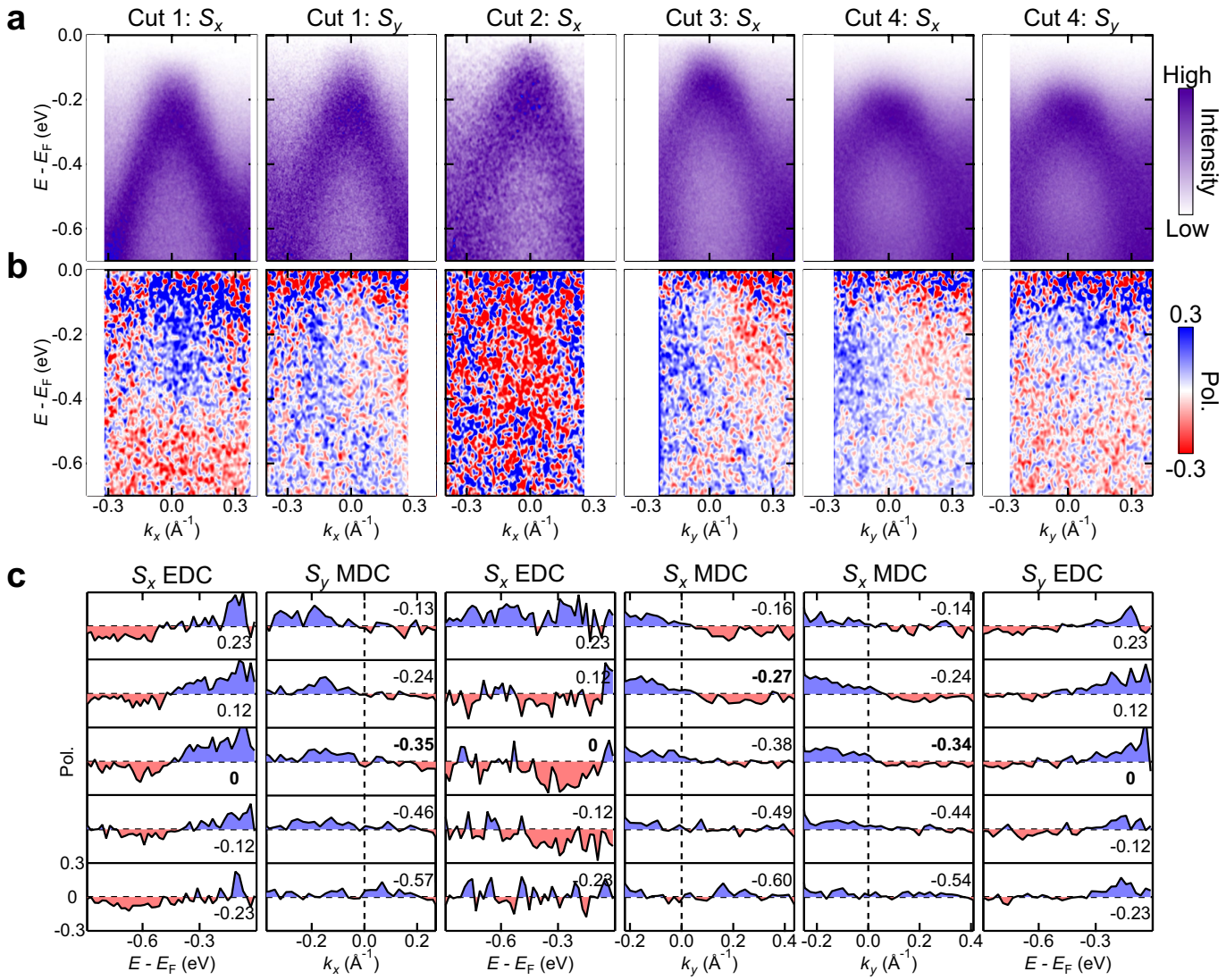

Extended Data Fig. 5 | Raw spin-resolved *E*–*k* images along Cuts 1–4 and corresponding polarization curves. a, Spin-integrated *E*–*k* images along Cuts 1–4 obtained by the spin-imaging ARPES system, shown in Fig. 2e–j. **b**, Corresponding raw spin-resolved *E*–*k* images. The difference between these images and those in Fig. 2 is that the data here are not multiplied by the spin-integrated intensity of the bands. In other words, these are the 'raw' spin-polarized data obtained with the image-type spin detector. **c**, Spin polarization curves of Cuts 1–4 at all measured *E*–*k* areas. From these images and polarization curves, the same conclusions as those in the main text can be drawn: the x (y) component of the spin-polarization vector is antisymmetric about $k_y = 0$ ($k_x = 0$). Furthermore, we see that non-vanishing spin polarization also exists in *E*–*k* areas that have 'no bands' (low spin-integrated ARPES intensity), which possibly comes from spin signals of vague electronic states or from bands at other k_z values (k_z broadening effect).

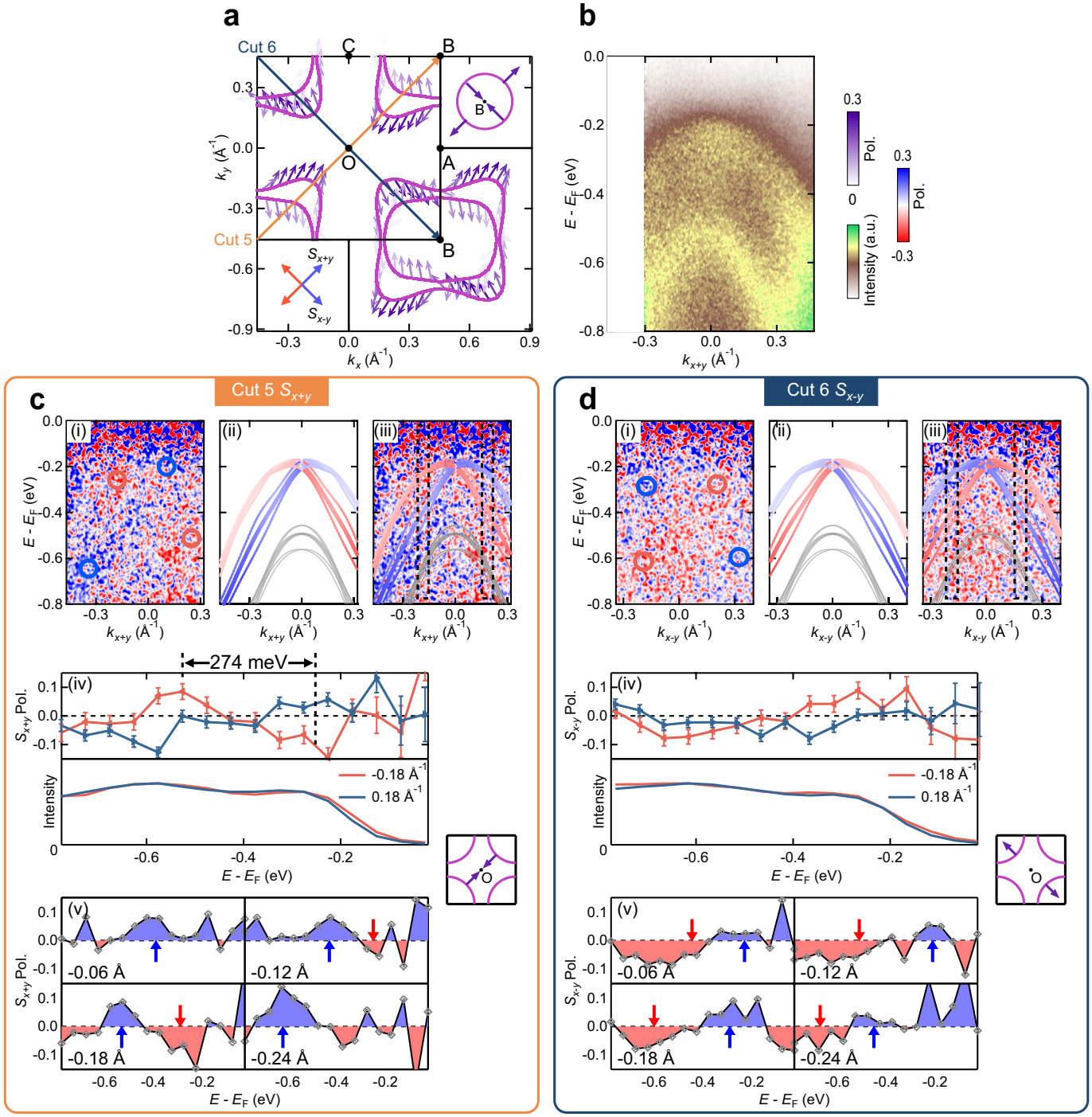

Extended Data Fig. 6 | Further evidence for the Dresselhaus-like in-plane spin texture. a, DFT-calculated spin-resolved CEC at $k_z = -0.2\pi/c$ and binding energy $E_B = 0.45$ eV. In-plane spins point mainly along $\pm S_{x+y}$ and $\pm S_{x-y}$, resembling the Dresselhaus configuration. The direction of $+S_{x+y}$ and $+S_{x-y}$ are defined along $k_x + k_y$ and $k_x - k_y$, respectively, shown in the bottom-left inset. The top-right inset depicts the schematic spin texture centred at point B. **b**, Spin-integrated ARPES band dispersion along Cut 5. Cuts 5 and 6 are defined in **a**; the bands along Cut 6 (not shown) seem the same. The observed bands exhibit two hole pockets and further intensity at $k = 0$ and $E_B = 0.4$ eV. **c**,**d**, S_{x+y}-resolved and S_{x-y}-resolved raw E–k cuts along Cuts 5 and 6. Blue/red circles highlight the regions with +/− polarizations. The SARPES results (i) vaguely corroborate with the DFT-calculated results (ii), which becomes more obvious by overlaying the calculated spin-resolved energy bands on the SARPES images (iii). iv, Polarization curves (top) and spin-integrated intensity curves (bottom) at $k = \pm 0.18$ Å^{-1}, integrated within the dashed rectangles in iii. Each point on a curve is an integrated intensity over a (E, k) range of (50 meV, 0.08 Å^{-1}). These spin-resolved EDCs reveal three important features. First, the S_{x+y} polarizations at $k_{x+y} = \pm 0.18$ Å^{-1} have opposite polarizations at the same binding energy. Second, the polarization at low binding energy (about 0.25 eV) and high binding energy (about 0.55 eV) is opposite. The corresponding S_{x-y} polarization of Cut 6 also exhibits these two features. Third, comparing the polarization curves at −0.18 Å^{-1} in Cuts 5 and 6, we find that their polarizations are opposite at the same binding energy. Extracted from the polarization curves, the energy scale of the spin splitting is about 274 ± 40 meV, which is in good agreement with the calculated 297 meV and is comparable with the well-known giant bulk Rashba effect[38]. v, Polarization curves versus momentum. We can trace the splitting along k and find that the $+S_{x+y}$ ($-S_{x-y}$) spin-polarized peaks of Cut 5 (Cut 6) move downward in energy when k moves away from O. In summary, our SARPES data along Cuts 5 and 6 reveal a Dresselhaus-like in-plane spin texture and ruled out a Rashba-like spin texture.

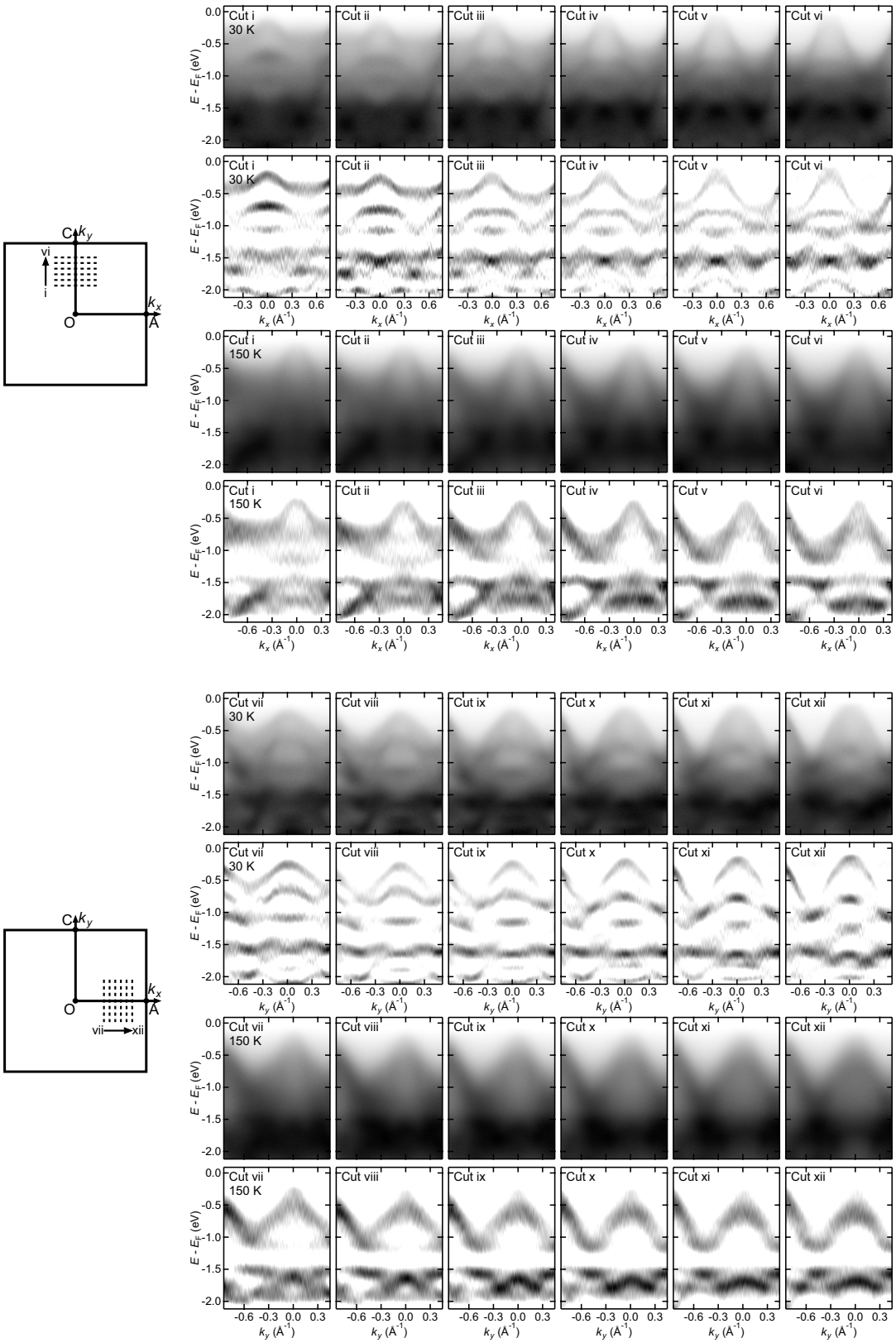

Extended Data Fig. 7 | Temperature dependence of the ARPES band structures. ARPES band dispersion along Cuts i–xii and corresponding second-derivative analysis along the energy direction at $T = 30$ K and 150 K, respectively. The positions of Cuts i–xii are marked in the schematic of the first Brillouin zone. Apart from the data shown in Fig. 4, here the band structure is also seen to undergo a non-rigid shift and several energy-band changes across the Néel temperature ($T_N = 87$ K).

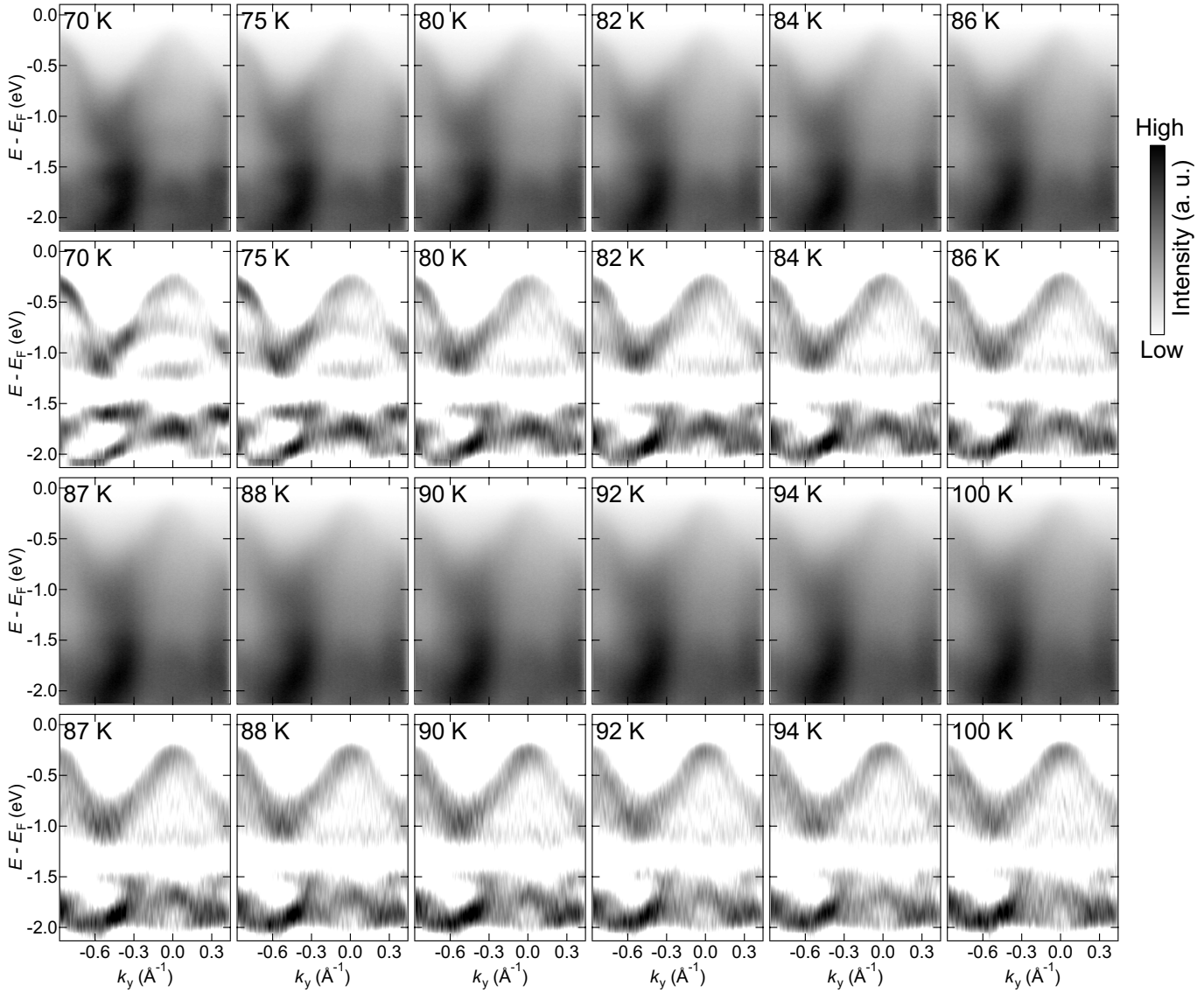

Extended Data Fig. 8 | Temperature-dependent electronic structure along Cut 3. ARPES band dispersion below and above T_N = 87 K and corresponding second-derivative analysis along the energy direction. The band structures are seen to undergo a structural modification associated with the AFM to paramagnetic transition.

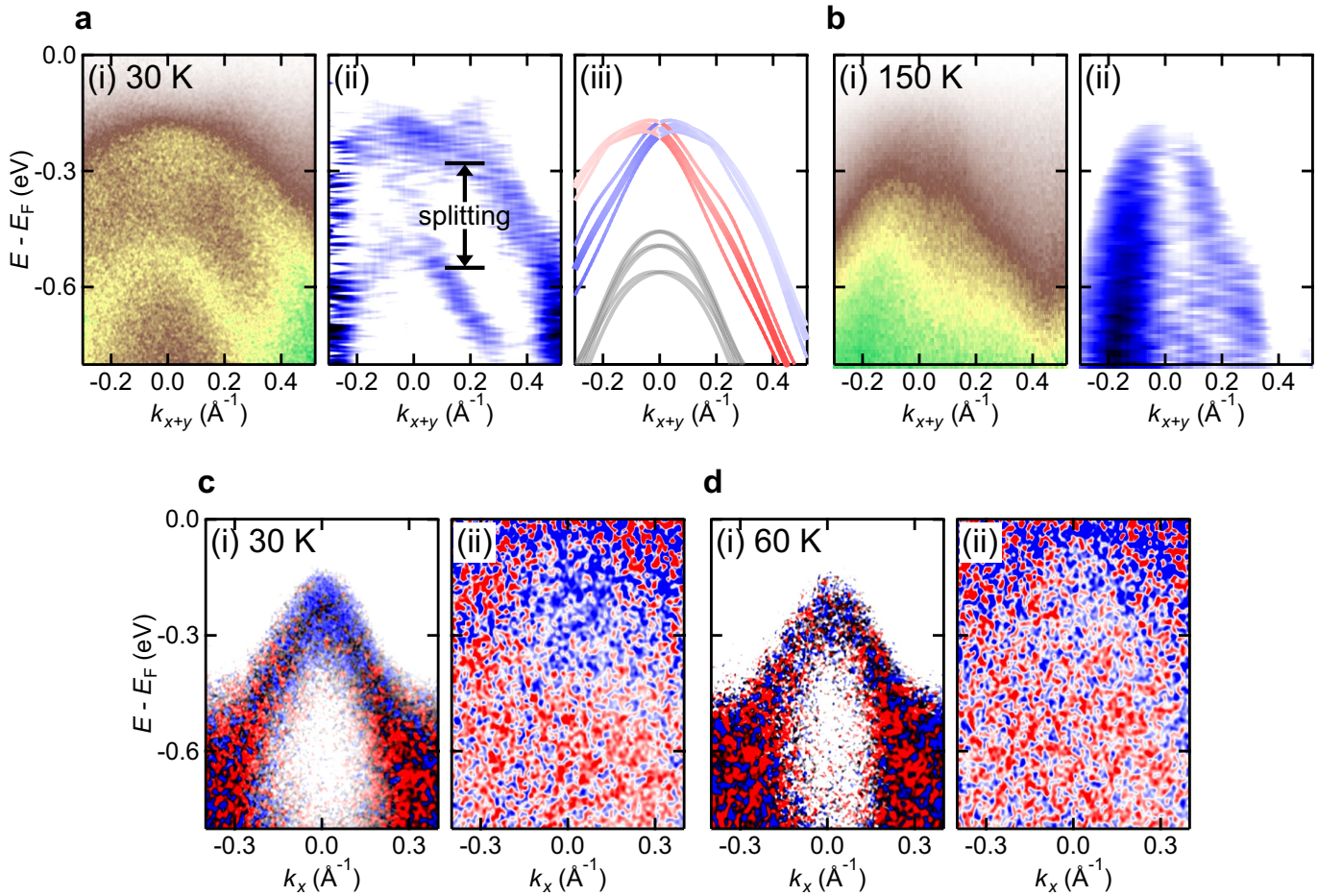

Extended Data Fig. 9 | Temperature evolution of the spin splitting and the spin-polarization signal. a,**b**, Temperature dependence of the band splitting: ARPES band dispersion along Cut 5 at 30 K and 150 K (i); corresponding second derivatives to the raw data (ii); and spin-polarized DFT bulk bands for the low-T AFM state (iii). The abrupt change of bands between the two temperatures is evident for the vanishing of spin splitting above T_N. **c**,**d**, S_x-resolved E–k images along Cut 1 and corresponding raw SARPES data. Data are taken at 30 K (**c**) and 60 K (**d**). Data in **c** and **d** are measured consecutively on the same sample with the same experimental settings and integration time. Because the bands at 30 K and 60 K, as well as the associated matrix elements, are not expected to change because they belong to the same magnetic phase, the decrease in spin polarization here is probably intrinsic, related to the origin of spin splitting.

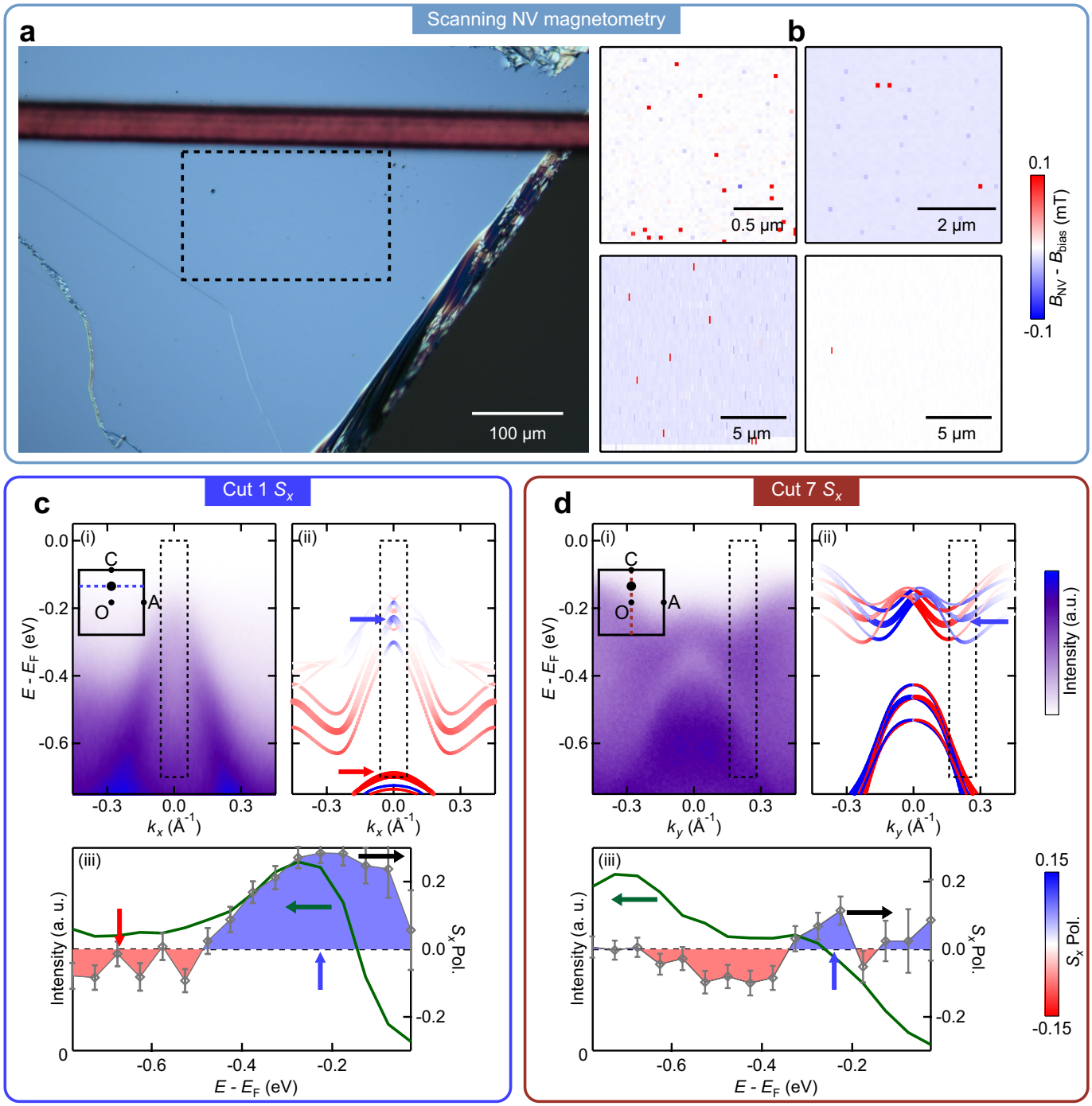

Extended Data Fig. 10 | Evidence for a large magnetic domain size. **a**,**b**, Evidence from cryogenic scanning NV magnetometry. **a**, A typical micrograph of the $MnTe_2$ sample. Four different areas, corresponding to **b**, are measured within the dashed rectangle. **b**, Stray magnetic fields along the NV centre axis (about 55° to the surface normal) measured at 2 K. The sample is scanned using a pulsed ODMR scheme (see Methods). The spatial resolution is set to about 30 nm. An external magnetic field of 0.6 mT is applied along the NV centre axis to lift the degeneracy of the NV ±1 spin states. No feature was detected within the measured length scales over a larger scan area (50 μm), indicating that the stray-field variations of the sample fall below the sensitivity threshold of the NV probe (2 μT/$\sqrt{\text{Hz}}$). Because the NV spin would detect non-vanishing magnetic fields contributed by domain walls, the measured feature in $MnTe_2$ suggests a uniform and large magnetic domain with no net magnetic-moment contributions[58,59]. **c**,**d**, Evidence from S_x-resolved electronic structures before and after rotating the sample by 90°. i, Spin-integrated E–k dispersion along Cuts 1 and 7 (defined in the insets). ii, Corresponding DFT-calculated S_x-resolved E–k dispersion. iii, Spectral intensity and S_x polarization at $(k_x, k_y) = (0, 0.5\pi/a)$ (large black dot in the insets) measured along Cuts 1 and 7. These curves are integrated within the dashed rectangles in i. The definition of S_x and error bars are the same as in Fig. 2. The S_x-polarization curves have the same sign at similar binding energies before and after rotating the sample by 90°, which is reproduced by DFT calculations (blue/red arrows). This is indicative of a magnetic domain size comparable with the size of the incident beam spot.

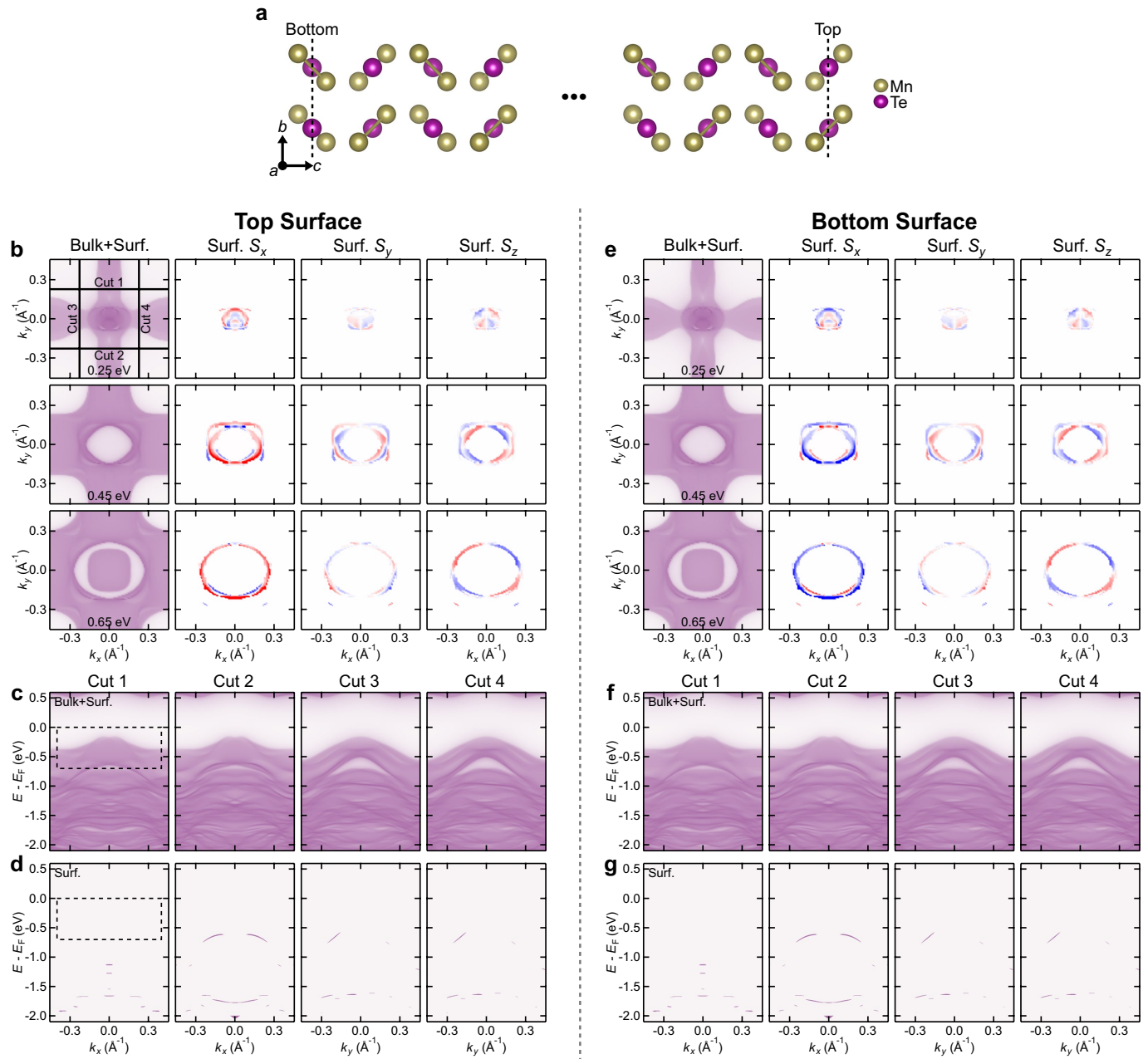

Extended Data Fig. 11 | DFT-calculated electronic structures from semi-infinite slab models. a, Calculation model with two different surfaces marked as 'top' and 'bottom'. Panels **b**–**d**/**e**–**g** show the calculated results on the top/bottom surface. **b**, Spin-integrated and spin-resolved CECs at binding energies E_B = 0.25, 0.45 and 0.65 eV, respectively. The spin-integrated CECs contain the spectral weights of both the bulk and the surface states. The spin-resolved CECs show the spectral weights of surface states only. At the three binding energies, there is almost no spin-polarized surface states at the positions of Cuts 1–4. **c**, Spin-integrated E–k dispersions along Cuts 1–4. These images contain the spectral weights of both the bulk and the surface states. **d**, Corresponding spin-integrated E–k dispersion of the surface states only. The dashed rectangles in first panel of **c** and **d** mark the ARPES-measured E–k region along Cuts 1–4 in Fig. 2. Clearly, there is almost no surface state in the areas we have measured. **e**–**g**, Results of the bottom surface, yielding the same conclusion. The data in this figure are evidences for the bulk nature of the spin-polarized bands in Fig. 2.

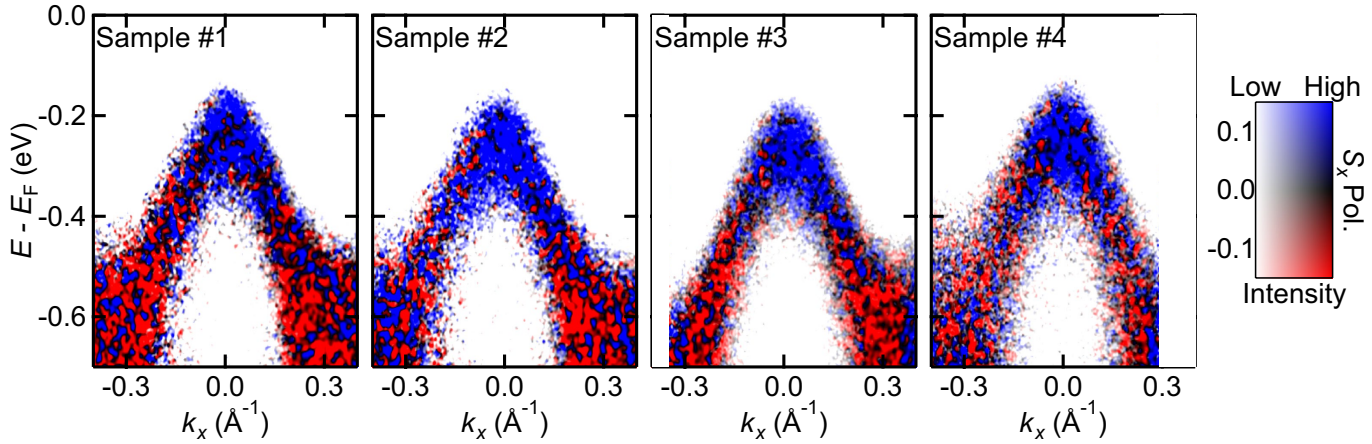

Extended Data Fig. 12 | Repeatability of the SARPES data. S_x-resolved ARPES maps on Cut 1 (Fig. 2e) are measured with four different samples. The experimental results are clearly reproducible.

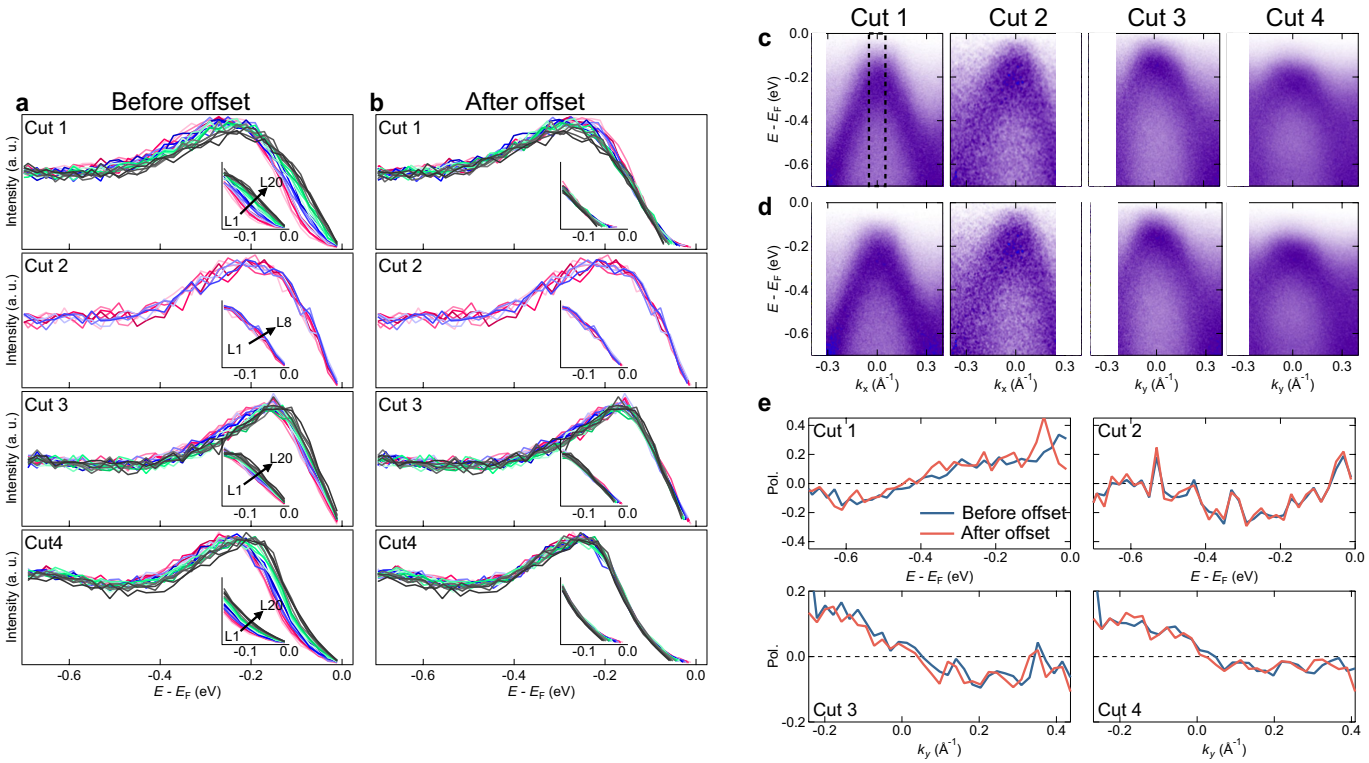

Extended Data Fig. 13 | EDCs at $k = 0$, band dispersions and S_x-polarization curves before and after an offset along the energy direction. This process eliminates the slight hole-doping effect caused by the slow but gradual ageing of the samples in the vacuum chamber. **a**, EDCs of Cuts 1–4 before the offset. The energy bands are found to shift rigidly upward along the energy direction with increasing loop number (measurement time). **b**, EDCs of Cuts 1–4 after the offset. The bands are offsetting downward referring to the first loop (L1), which represents the pristine energy positions of the bands. The EDCs are taken at $k = 0$ Å^{-1}, integrated within the rectangles in the first panel of **c** and **d**. **c**,**d**, Band dispersions of Cuts 1–4 before and after the offset, respectively. **e**, S_x-polarization curves before and after the offset. The integrated positions are the same as Fig. 2e–h. One can find that the offsetting procedure introduced no qualitative difference to the spin polarization, except for a slight change of polarization magnitude near the Fermi level. The main conclusion of the paper is valid regardless of using the data before or after the offset.

Extended Data Table 1 | The differences in the spin splitting originating from SOC and AFM magnetic order in $MnTe_2$ encompass variations in symmetry, k_z dependence, temperature dependence, $k \cdot p$ models and permissible spin texture types

Origin	SOC (surface)		AFM (bulk)	
Symmetry group	*Pc1'*		*Pa-3*	
Time-reversal	✓		✘	
Space-inversion	✘		✓	
k_z-dependent	✘		✓	
T-dependent	✘		✓	
Allowed spin splitting $k \cdot p$ terms	Odd only		Even only	
$k \cdot p$ model	$k_y\sigma_x - k_x\sigma_y$	$k_y\sigma_x + k_x\sigma_y$	$k_z(k_y\sigma_x + k_x\sigma_y)$	
Spin texture type	Rashba (Linear)	Dresselhaus (Linear)	Plaid-like (Quadratic)	
			($k_z > 0$)	($k_z < 0$)
Spin texture in k_x-k_y plane	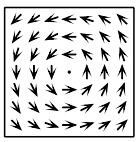	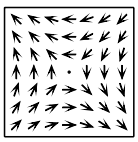	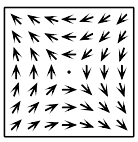	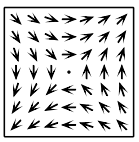

Extended Data Table 2 | Little group and the allowable spin splitting of bands at different *k* positions

Position	High symmetry line	Little group	Spin splitting
Γ (0, 0, 0)	Not a line	m-3	no
X (0, 1/2, 0)	Not a line	mmm	no
M (1/2, 1/2, 0)	Not a line	mmm	no
R (1/2, 1/2, 1/2)	Not a line	m-3	no
X1 (1/2, 0, 0)	Not a line	mmm	no
Δ (0, v, 0)	Γ - X	m2m	no
Z (u, 1/2, 0)	X - M	2mm	no
Σ (u, u, 0)	M - Γ	..m	S_z
Λ (u, u, u)	Γ - R	3	S_x, S_y, S_z
S (u, 1/2, u)	R - X	.m.	S_y
T (1/2, 1/2, w)	R - M	mm2	no
ZA (1/2, u, 0)	M - X1	m2m	no
Δ’ (u, 0, 0)	X1 - Γ	2mm	no
P1 (u, v, 0)	Γ- X - M plane	..m	S_z
O (0, 0, 1/5)	Not a line	mm2	no
P2 (u, 0, 1/5)	O - A	.m.	S_y
A (1/2, 0, 1/5)	Not a line	mm2	no
P3 (1/2, v, 1/5)	A - B	m..	S_x
B (1/2, 1/2, 1/5)	Not a line	mm2	no
P4 (u, u, 1/5)	B - O	1	S_x, S_y, S_z
GP (u, v, w)	General points	1	S_x, S_y, S_z

Splitting of all spin components S_x, S_y and S_z are allowed in general points. Little groups are ordered with respect to the three axes, for example, 2mm at the *Z* point represents C_{2x}, M_y and M_z.